UNIVERSITY OF OTTAWA

OTTAWA-CARLETON INSTITUTE FOR MECHANICAL AND AEROSPACE ENGINEERING

Pupil Tracking and Control of a Laser Based Power System for a Vision Restoring Retinal Implant

Author:
Nathaniel Mailhot

Supervisor:
Davide Spinello
Co-supervisor:
Karin Hinzer

A thesis submitted in partial fulfillment of the requirements for the Master of Applied Science degree
in
Mechanical Engineering

uOttawa

© Nathaniel Mailhot, Ottawa, Canada, 2019

Pupil Tracking and Control of a Laser Based Power System for a Vision Restoring Retinal Implant

Nathaniel Mailhot

Abstract

For elderly Canadians, the prevalence of vision impairment caused by degenerative retinal pathologies, such as age-related macular degeneration and retinitis pigmentosa, is at an occurrence rate of 14 percent, and on the rise. It has been shown that visual function can be restored by electrically stimulating intact retinal tissue with an array of micro-electrodes with suitable signals. Commercial retinal implants carrying such a micro-electrode array achieve this, but to date must receive power and data over copper wire cable passing through a permanent surgical incision in the eye wall (sclera). This project is defined by a collaboration with iBIONICS, who are developing retinal implants for treatment of such conditions. iBIONICS has developed the Diamond Eye retinal implant, along with several technology sub-systems to form a comprehensive and viable medical solution. Notably, the Diamond Eye system can be powered wirelessly, with no need for a permanent surgical incision.

The thesis work is focused on the formulation, simulation and hardware demonstration of a powering system, mounted on glasses frame, for a retinal implant. The system includes a Micro-Electro-Mechanical System (MEMS) mirror that directs a laser beam to the implant through the pupil opening. The work presented here is built on two main components: an iterative predictor-corrector algorithm (Kalman filter) that estimates pupil coordinates from measurements provided by an image-based eye tracking algorithm; and an misalignment compensation algorithm that maps eye pupil coordinates into mirror coordinates, and compensates for misalignment caused by rigid body motions of the glasses lens mirror and the MEMS mirror with respect to the eye. Pupil tracker and misalignment compensation control performance are illustrated through simulated scenarios. The project also involves the development of a hardware prototype that is used to test algorithms and related software.

Dedication

This is dedicated to Hailey Willams.

Thank you for keeping me focused when I am the most distracted, and distracted when I am the most focused.

Acknowledgments

I would like to thank my supervisor Davide Spinello for introducing me to the wonderful world of the academic engineering pursuit, and giving me the opportunity to learn more than I could have without. I am grateful to him for all that I have had the opportunity to experience in my time thus far. In the last three years of working with you, I am left with the feeling that I have only just begun.

To my teammates from the SUNLAB at uOttawa: my co-supervisor Karin Hinzer, Ross Cheriton, John Cook, Kaustubh Vyas and Javad Fattahi. Thank you all for your support. It has been an absolute pleasure having the chance to work with these bright, joyful minds.

To the members of iBIONICS: Anne Bruneau, Grant Dawson, Suzanne Grant and Steven Prawer. Thank you for all the insight, support and hospitality you provided me during our collaboration. It has been a pleasure.

To two of my favourite professors with the University of Ottawa, Natalie Baddour and Eric Lanteigne, thank you. You both helped me negotiate through the tough senior years of my bachelor's degree, and now a master's degree too. You reminded me to stay focused, play my cards right, see the bigger picture, and above all else and enjoy my studies.

Finally, to my parents. Thank you for supporting my life long decision to be stubborn, question everything, and plot my own course in life.

Most of our obstacles would melt away if, instead of cowering before them, we should make up our minds to walk boldly through them. Orison Swett Marden

Contents

List of Figures

List of Tables

Chapter 1

Introduction

1.1 Background: Visual Prosthesis by Retinal Implants

Incurable retinal disease, most notably Age-related Macular Degeneration (AMD) and Retinitis Pigmentosa (RP), are some of the most common causes for blindness globally [1, 2, 3]. AMD is a progressive illness that affects as many as 20 percent of Canadian citizens above the age of 50, where as RP is a set of inheritable dystrophies ailments that is age indiscriminate. Both diseases affect the light sensing cell structure of the retina, while leaving the underlying tissue and optic nerves unscathed. Since the 1950's, vision researchers have shown that it is possible to electrically stimulate the neural pathways below the retina that remain healthy regardless of the illness itself[4, 5]. The net result is that the otherwise blind individual can perceive some visual stimulus. A schematic showing the concept of some typical eye implants utilizing an array of electrodes to stimulate the visual neurons is shown in Figure 1.1 [6].

The notion of a vision prosthesis that utilizes the concept of stimulating the visual pathways below the damaged retina is being developed by several research teams in academic and commercial settings [7, 8, 9]. Of note, the retinal implants developed by Second Sight Medical Products and Retina Implant AG have reached the clinical trials, where their visual prosthesis devices have been implanted and are functional within vision impaired individuals. With both products, patients have described improved visual sensing ability, being able to detect household objects, horizontal motions and even large letters. The patients who chose to continue to use the implant along with standard vision impairment aids after the clinical trials are more independent than before the surgery.

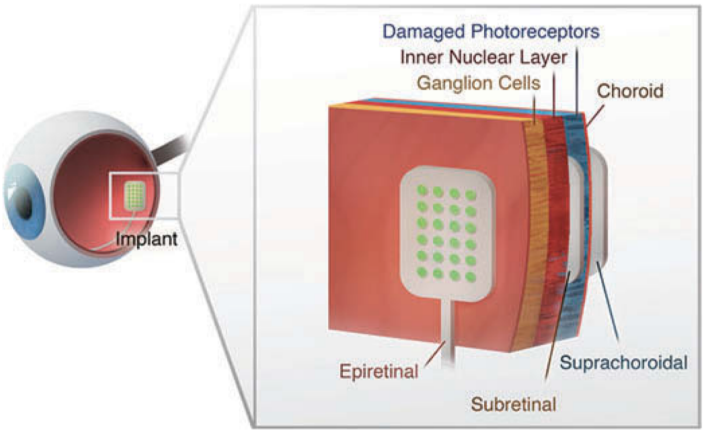

Figure 1.1: An overview of the tissue responsible for capturing vision information is shown, along with different locations where an electrode array may stimulate the cells to produce a visual response.

A design problem that faces current retinal implants is the necessity for the device to be connected to the external world by a wire to receive power and electrode stimulation sequence data. This takes the form of additional implanted hardware, and an increase in surgery complexity. There are a few different approaches to accomplish this. For example, with the Second Sight Argus II implant, a permanent incision in the eye wall allows for a direct wire to a radio frequency or magnetic induction receiver that is attached to the outside of the eye globe. For the Alpha-IMS implant from Retina Implant AG, a cable runs through the back of the eye, through a portion of the skull, and is fed under the thin muscle tissue below the skin to behind the ear, where a wireless power receiver coil is implanted. The permanent surgical modifications required to accommodate the wired implants lead to additional in-surgery time and post-surgery monitoring, as well as an increased risk for damage to the device or infection risk for the patient.

Wireless retinal implants (i.e. that do not need a hardline connection from the implant to outside the eye globe) generally require less implanted hardware, and reduced surgical time. Furthermore, the risk of adverse medical conditions to the patient due to the wired connection would be eliminated. Wireless power delivery could be provided by short range wireless transmission of power as seen in the EPI-RET3, or by a laser power delivery scheme as seen in the Diamond Eye from iBIONICS[10, 11, 12].To make a comparison, the current state of the art successful wired retinal implant system, the Argus II, is shown in Figure 1.2 [13], and the concept for the wireless Diamond Eye implant is shown in Figure 1.3. Note that with the fully wireless implant, the overall package size is significantly reduced,

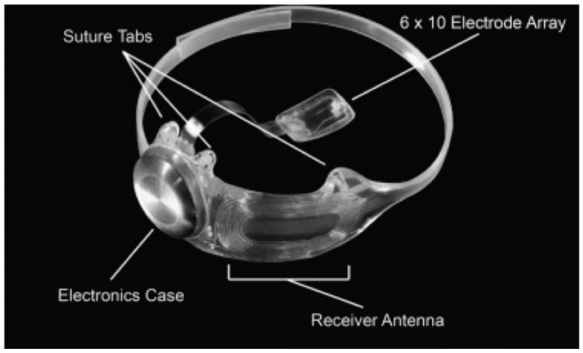

Figure 1.2: Argus II internal electronic components, electrode array and suture mounting design. The ribbon connecting the electrode array to the electronics case is fed through a permanent incision of the sclera.

and there is no need for an incision in the sclera nor any electronics resting on the outer eye wall.

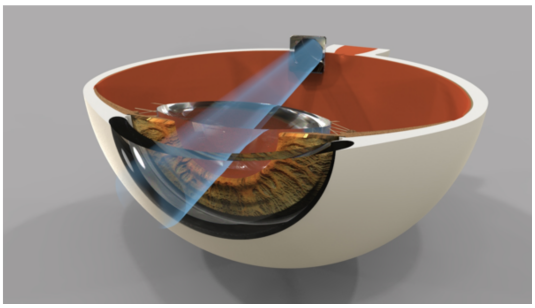

Figure 1.3: Concept of the Diamond eye retinal implant. A laser is directed through the pupil to a PV cell that receives power and visual field information. (Provided by iBIONICS).

1.2 Motivation

The ideal retinal implant would require minimal surgery time, be simple to implant, and would have as little hardware as possible. By moving to a wirelessly powered implant design, the additional hardware complexity introduced by a wired power and data source would be reduced or removed. A wireless power system is one of the primary design goals for the Diamond Eye from iBIONICS.

The Diamond Eye is designed to require as little power hardware as possible for the implanted package. A photovoltaic cell captures power from a low power directed laser, and an embedded photodiode receives visual scene information sent by data modulation of the laser pulse. Both the photodiode and photovoltaic cell

are integrated on top of the ASIC contained within the Diamond package, requiring no other implanted hardware. The total surface area of the diamond package is 5 mm square. A prototype of the diamond eye microelectronics package is show in Figure 1.4.

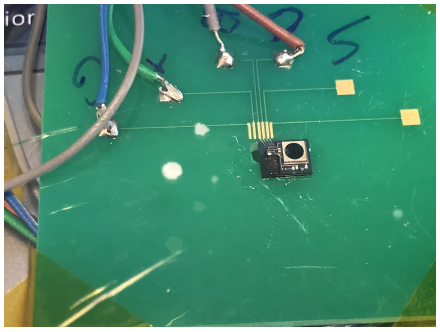

Figure 1.4: A picture of the Diamond Eye prototype ASIC. Here, the PV cell (the black circle within the silver square) is 2 mm in diameter.

Other methods may be considered to provide power and scene information to a retinal implant, wirelessly. For example, the EPI-RET3 implant uses a short range wireless power transmitter and receiver setup. The receiver is an additional package implanted within the eye that replaces the natural lens of the patient, to be as close as possible to the external transmitter. Ultimately, short range power transduction is limited by the proximity between the transmitter and the receiver, as well as objects laying in between. The EPI-RET3 is limited by the inverse square law, requiring exceedingly more power as necessary transmission range increases, while also contending with any biological tissue in the way.

A truly wireless retinal eye implant would provide an improved visual prosthesis design that reduces the surgical complexity and risk of medical complications that are present with current in development wired or pseudo-wired retinal implants. The Diamond Eye Retinal Implant developed by iBIONICS would capture both energy and data from a laser beam targeted through the pupil of the patient. To steer the laser, a control system must be presented that is able to consistently target the PV cell on the implant through eye motions. Ideally, the laser light would continuously fall onto the implant, providing sufficient power to stimulate the electrodes for all circumstances except for a blink event.

Herein lies the focus of this work: the need to conceptualize and develop a laser steering control system that would ensure consistent power delivery to the Diamond Eye implant. The controlled laser steering system must remain small such that it is able to be mounted to a glasses frame worn by the patient. It must

consistently target the Diamond Eye implant, to ensure consistent power delivery during stimulation. The system needs to be able to respond to changes in the orientation of the patient's eye, while also adapting to geometric disturbances of the glasses frame that cause misalignment.

This work was partially funded by the two Canadian academic-industry collaborative federal and provincial grants, the National Science and Engineering Research Council (NSERC) ENGAGE, and Ontario Centres of Excellence (OCE) VIP:1 GRANT.

1.3 Objectives of Thesis

Design: Present the concept of a laser steering method that utilizes a frame mounted, micro-electro-mechanical system (MEMS) mirror to control the targeting of a laser beam to supply power to a wireless retinal implant.

Tracking: Validate that the system can adequately redirect the laser beam within a sufficient window of time such that the laser target is maintained during eye motion, and recovers after blink events.

Misalignment adaptation: Characterize the misalignment compensation control algorithm for the implant tracking system such that intended laser target on the implant is maintained in the event of the glasses frame being subjected to a geometric disturbance that causes the misalignment of the laser beam.

Sufficient power delivery: Prove the feasibility of the system to provide adequate power to the implant during real eye motion events through a computer model of the system.

1.4 Thesis Outline

The solution for a wireless power delivery system by the use of a directed laser is main topic presented within this work. The solution is presented with the following structure:

In Chapter 2, a literature review presents the background and context of the work, in particular the function, development and history of visual prosthesis and retinal implant technology. The review introduces visual prosthesis technology, the associated vision loss pathologies addressed by visual prosthesis, and then

discusses with some breadth the current state of retinal implant technology development. A focus is put on current retinal implants in clinical trials, and the issues presented by wired retinal implants. A review on the dynamics of human eye motion and eye tracking is presented expressly to provide context for the design requirement of the wireless implant tracking system.

Chapter 3 presents the eye tracking and laser targeting system that provides the MEMS mirror with the desired laser target position, to wirelessly power the retinal implant. A predictive tracking algorithm is presented that compensates for error prone camera-based eye position measurements with a low sample rate. A computer simulation model is presented that demonstrates the resulting power received by the retinal implant as the laser target and eye itself move in time, changing the amount of laser light incident on the photo-voltaic cell of the implant. The eye motion used within the simulation is captured from video samples of real eye motion. These results are compared to an experimental prototype system developed by the University of Ottawa in collaboration with iBIONICS.

Chapter 4 presents the geometric model for the glasses frame mounted system. The physical layout of the optical system is present, with a focus on the ellipsoidal lens used for consistent laser redirection from the MEMS mirror to the photo-voltaic cell of the implant. The misalignment compensation MEMS mirror control algorithm is presented. The function of this control algorithm is to determine the target-able region of the implant during a physical disturbance, resulting in misalignment of the glasses frame system. Examples are provided that demonstrate the control actions response to different cases of geometric misalignment of the glasses frame, due to a horizontal rotational disturbance.

Chapter 5 contains a brief summary of the work, results centered around the viability of the proposed wireless implant tracking solution, and future possible improvements to the designed solution's control system.

Chapter 2

Literature Review

2.1 Vision loss by retinal pathologies and restoration

2.1.1 Retinitis pigmentosa and macular degeneration

Vision restoration via a bionic eye is already a market reality and is analogous to other proven commercial medical products for sensory system restoration [14, 15]. The most common analogue is the Cochlear implant, used in hearing restoration applications. The Cochlear implant functions by applying electric signals that encode auditory information directly to the cochlear nerve . With modern cochlear implants, patients enjoy a restored auditory sense, resulting in a significant quality of life improvement for functionally deaf recipients [16, 17]. The success of the cochlear implant is held as an inspiration for a visual prosthesis system, which can restore vision to the otherwise functionally blind.

Age related Macular Degeneration (AMD) and Retinitis Pigmentosa (RP) are the two main categories of incurable vision loss pathologies that are the targets for retinal implants[1]. AMD is characterized by the progressive loss of central vision due to age related degenerative changes of the macula (the center of the retina[2, 18]. As the disease progresses, a larger surface area of the macula becomes scarred or atrophied, resulting in further central vision loss. A time lapse showing the progression of the disease is shown in Figure 2.1 [18]. AMD is the most common, incurable cause of vision loss afflicting the elderly worldwide, with as many as 50 million. It is predicting that AMD affects 9 percent of the global population when considering all age groups. RP describes a set of common diseases where patients experience a progressive loss in photoreceptor cells [3]. The impact of RP can range from a loss of low light vision, to a full loss of side and central vision.

RP is predicted to affect one million people worldwide.

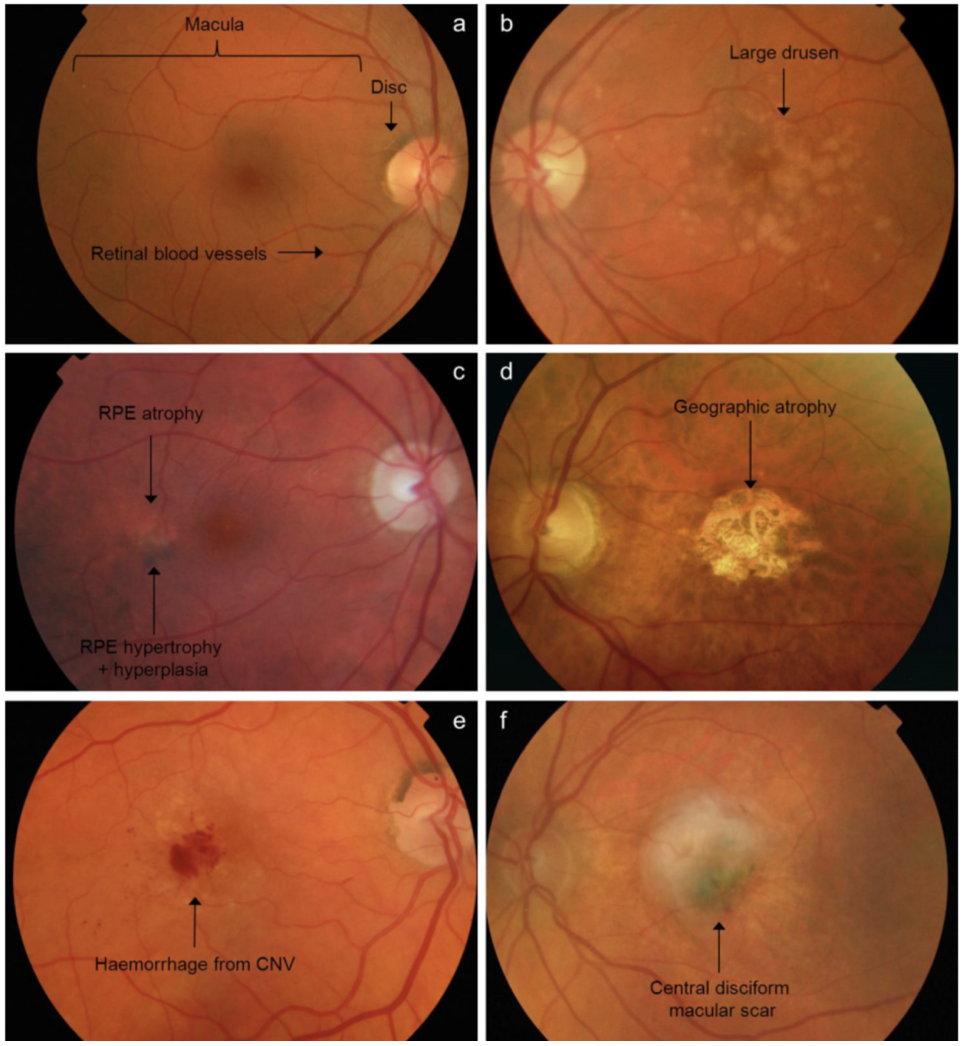

Figure 2.1: The progression of macular degeneration. The series of images capture time lapse of a patient progressing from healthy tissue to permanently scarred macular tissue.

To restore vision to a blind individual, the scene information of the world must be received, and then processed by the individual while bypassing the elements of their ocular-neural system that are nonfunctional. Methods to do so include repairing or replacing the compromised biological systems, or surgically interfacing an implant to the retina, the optical nerve or directly to the visual cortex [9, 13, 14, 19]. The three avenues for visual prosthesis (retinal, optical nerve, and cortical) are listed in order of how 'downstream' they lie from initial light information collection to the brain processing the signals. Likewise, the complexity of the biomedical implant interface increases as you go downstream. Most development has been

focused on retinal implants, considered to be the simplest, most surgically realizable prosthesis method that can account for a wide range of common vision loss pathologies.

The primary method most widely developed to restore vision to those affected by retinal disease is by electrical stimulation of the nerve system connected to the retinal ganglion cells. It has been demonstrated that individuals without vision for decades due to retinitis pigmentosa or macular degeneration are capable of sensing light stimulus when an electric current is applied on the retinal tissue [4, 5]. This fundamental notion acts as the foundation for the development of retinal prosthesis implants that utilize a microelectrode array to stimulate the ganglion cells, resulting in visual stimulus being detected by the patient.

2.2 Retinal prosthesis systems

2.2.1 Current state of the art

Current in development retinal prosthesis systems employ the same core concept of energizing a microelectrode array to stimulate the underlying ganglion cells, to restore vision to the patient [7, 8, 9]. Major differences between each implant lie in details on the electrode resolution, size and spacing, the location of the implant (epiretinal or subretinal), and the interface of the implant to the external power and data system. Visual image information is provided by either external camera systems with some video processing, or with a multiphotodiode array that absorbs light and stimulates corresponding electrodes. At the time of writing, two retinal implants (Argus II and Alpha-IMS) have been approved for in human clinical studies. A comparison reproduced from [7] describes a selection of the most developed retinal eye implants, along with other visual prosthetic solutions is shown in Figure 2.2.

The Argus II (Second Sight) was the first device approved for clinical trials within both the US and EU. The Argus II consist of an Application Specific Internal Circuit (ASIC) and a 60-microelectrode array, connected through the sclera by a wire to an RF coil mounted to the surface of the eye globe. A picture of the internals is shown by Figure 1.2. Vision information captured by a small camera, and power is transmitted by induction from an external, glasses mounted power system to the internal system. A picture of the external system is shown in Figure 2.3 [13].

Argus II patients have demonstrated the ability to follow white lines along a

Visual prostheses	Retinal prostheses				Optic nerve head prostheses	Cortical prostheses
	Argus® II	Alpha-IMS	IMI, IRIS	EPI-RET 3 ('wireless' implant)		
Image capture	Extrinsic video camera	Intrinsic optical system	Extrinsic video camera	Extrinsic video camera	Extrinsic video camera	Extrinsic video camera
Light waves transduction into electrical signals	Extrinsic conversion by an external VPU	Intrinsic conversion by direct activation of micro-photo-diodes (MPDA)	Extrinsic conversion by an external processing unit	Extrinsic conversion by an external processing unit	Extrinsic conversion by an external processing unit	Extrinsic conversion by an external processing unit
Number of electrodes	60	1500 micro-phorodiodes, each connected to an amplifier and electrode	61	25	Spiral nerve cuff (MiViP); 3 (AV-DONE): 16	Dobelle: 64 Normann: 100
Field of vision	Up to 20°	11° × 11°	Up to 40°	Not available	14° × 41°	Not available
Site of stimuli	Inner retina with epiretinal electrodes	Outer retina with subretinal electrodes	Inner retina with epiretinal electrodes	Inner retina with epiretinal electrodes	Optic nerve head	Striate cortex of occipital lobe
Visual processing	Extrinsic processing by computer algorithms	Intrinsic intra-retinal processing	Extrinsic processing by computer algorithms	Extrinsic processing by computer algorithms	Extrinsic processing by computer algorithms	Extrinsic processing by computer algorithms
Status	Commercially available in Europe (CE mark March 2011) and the USA (FDA approval February 2013). Trials identifier: NCT01490827	Commercially available in Europe (CE mark in July 2013). Trials identifier: NCT01024803	Phase II clinical trial commenced January 2007. Clinical Trials identifier: NCT00427180	Completed acute clinical study. Awaiting further development and approval for chronic study	Experiments performed on volunteer human subjects	Experiments performed on volunteer human subjects

Figure 2.2: Mechanisms and development stages of different visual prosthesis systems.

dark floor, distinguish some shapes, and more accurately identify large letters with the implant powered than without [20]. Visual acuity is comparable to 20/1262. The requirement for a permanent sclera incision to connect the implant to the power source by wire raises the continued risk of infection, leading to serious ad-

Figure 2.3: Argus II external system consist of a camera mounted on a glasses frame along with the power and data induction coil. Power and information is provided by an external waist mounted unit.

verse events during clinical test [6].

The Alpha-IMS (Retina Implant AG) was approved for clinical trials within the EU and Hong Kong. The Alpha-IMS implant is unique in that it utilizes a Micro Photodiode Array (MPDA) to capture the local light that would otherwise land on the retina below [21]. The activated portion of the MPDA is amplified and transmitted to the electrodes that are directly below. The device itself is implanted within the subretinal tissues, requiring a more intricate surgery than in comparison to the Argus II [13]. Clinical trial patients were able to read letters with a visual acuity of 20/546, as well as detect motion, and recognize household objects. The implant provided a 11-degree field of view. Stimulations occurred at a rate of 5 to 7 Hz due to the operational constraint of the MPDA. The MPDA requires an external connection to a power source to amplify the transmitted light signals. This is provided in a similar fashion to other eye implants, where a wire connects the eye implant to the external device.

For the Alpha-IMS implant power amplification, a wire is put through the back-eye wall, through the skull, under the skin to behind the ear, where an inductive coil receives power. A set of images showing the full implant can be seen in Figure 2.4 [21]. Complications have arisen during clinical trials of the system. A se-

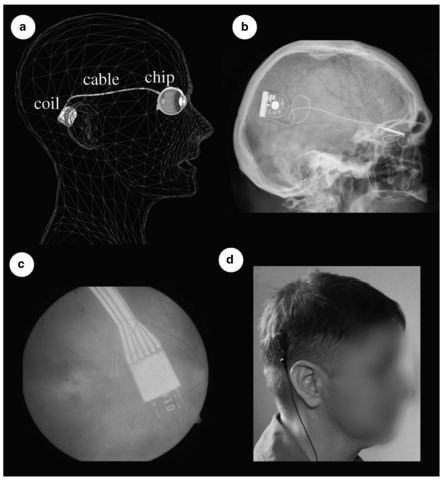

Figure 2.4: The Alpha-IMS implant: 1. A schematic of the implant is shown, 2. An X-Ray image of the implant within the patient, 3. The electrode array embedded on retina of the patient, 4. A picture of the patient, with the external power connection entering behind the ear.

rious adverse event affected patients, where the implant caused sub-retinal bleeding, and increased intraocular pressure [6]. With one patient, the implant touched the optic nerve during surgery, resulting in permanent damage and loss of light detection.

2.2.2 Wireless retinal implants

Retinal implants that use a wired power and data source require additional power transmission electrical components, and a more complex surgery to connect the implant to the external power source. The presence of a permanent eye wall incision, as well as additional extra-ocular hardware may lead to increased infection risk along with other complications for the patient. It would be considered ideal if the retinal implant is as small as possible, while requiring minimal invasive surgery. There are two retinal implants in development that are designed to receive power and scene information wirelessly: EPI-RET3, and the Diamond Eye.

EPIRET3 of the Epi-Ret Project, pioneered by Rolf Eckmiller at the University of Bonn, implements a radio frequency transmitter and receiver setup to transmit both power and data[10]. The receiver coil and stimulation chip is installed as a replacement for the patients eye lens, and connected to the retinal electrode array by a thin micro cable laid along the eye wall. The device itself was implanted into the eyes of six legally blind patients, who reported sensing dots, lines and arcs of circles. It was reported that different orientations of the electrodes would result

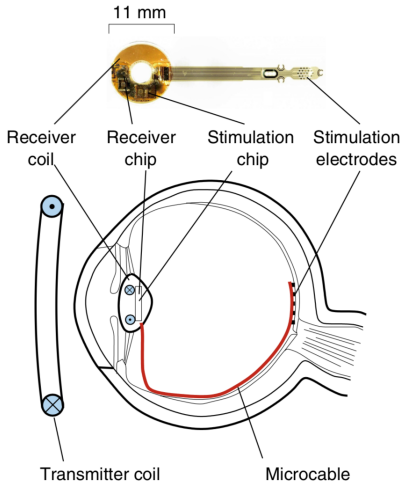

Figure 2.5: An implantation schematic of the EPIRET3. At the top of the image, a top down picture of the actual implant is shown.

in different orientations of the sensed visual stimulus. A schematic showing the implantation of the EPIRET3 Implant can be seen in Figure 2.5 [10].

The Diamond Eye developed by iBIONICS, pioneered by Steven Prawer of the University of Melbourne, is a currently in development wireless implant [11, 12]. The Diamond Eye consist of a small, hermetically sealed diamond package that integrates the electrodes directly into the diamond itself. The package contains the stimulation ASIC and a PV cell array, to receive power and scene information by a directed laser that can provide sufficient power to the system for stimulation, while also being under powered to not damage the internal eye tissue. The Diamond Eye implant is the least invasive of all retinal implants studied, due to being both the smallest of all stimulation electrode packages and requiring no additional power transmission hardware. A concept of the Diamond Eye implanted to a retina is shown in Figure 1.3. A picture of the protoype application specific integrated circuit (ASIC) for the Diamond eye, with included photovoltaic cell is show in Figure 1.4.

2.3 Tracking human eye motion

2.3.1 The visual field

The mechanics of human eye motion are defined by the distribution of photoreceptor cells on the retinal surface. The retina allows for a detectable horizontal field

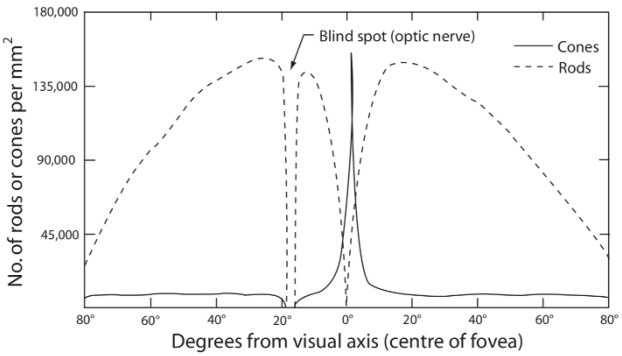

Figure 2.6: Distribution of photoreceptors within the human retina 2.6.

of view of approximately 180 degrees. However, the density of photoreceptor cells significantly decreases from the center of the retina towards the outer radius [22]. Human vision acuity sharply peaks within the central 2 degrees of visual field, corresponding to the photoreceptors of the most densely packed region the center of the retina, named the foveal region. The plot of the distribution of photoreceptor cells as a function of the radius from the center of the visual field is shown in Figure 2.6 [23].

Beyond the foveal region, visual acuity drops by as much as 50%, decreasing further along the peripheral, where visual perception is limited to the sensing of motions or light intensity changes [24]. The relative visual acuity of a region of the visual field as a function of eccentricity to the center of the visual field is shown in Figure 2.7 [25].

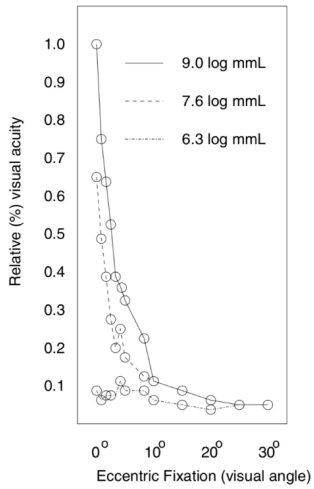

Figure 2.7: Relative visual acuity as a function of visual angle.

The high visual acuity of the foveal region necessitates that human eye must

rapidly fixate along objects of interest to capture important detail of the environment. Therefore, the human visual system functions to move the visual focus to areas of interest, such that the system may observe the object of interest in high detail [26]. Our perception of the visual field is a pieced together by successive observed areas of interest of foveal vision, with little reliance on the lower quality non-foveal visual field [22, 27, 28]. Eye motion acts to piece together important information from the visual field by successive, brief focusing the foveal region on different points of interest. A set of several eye motion samples is shown in Figure 2.8, demonstrating the scan path phenomena of the subjects attention as they observe the image [22].

2.3.2 Large eye motion and fixation

Large scale position change eye motion is considered to have 3 distinct primary modes, described as follows [26]:

Saccades: The dominant eye motion mode used to move the focus of the foveal region. They are characterized by rapid, linear motion that flicks from on point to the next. Typical saccades occur with a duration of between 10 to 100 milliseconds, with a displacement of the visual field focus of up to 45 degrees. At most, the highest amplitude saccades occur at maximum speed of 700 degrees per second. Saccades have extremely sudden acceleration and negative acceleration during the beginning and the end of the motion, allowing them to be modelled as simple linear ballistic motion. Due to the high speeds of saccades, all visual information that would be received during the motion by the brain is suppressed, resulting in the effective temporary blindness [29, 30]. A set of typical saccade amplitude profiles from a patient, showing the relationship between the velocity of a saccade to its duration is shown in Figure 2.9 [31].

Smooth pursuits: Motion mode that occurs when a point of interest is undergoing continuous linear motion. The motion is significantly more slow than saccadic motions, such that visual information of the object of interest is not suppressed. The eye acts to match the speed of the object.

Vergence: Motion mode that moves each eye in a correlated, yet different way such that visual focus may be shifted to a subject that is closer or further

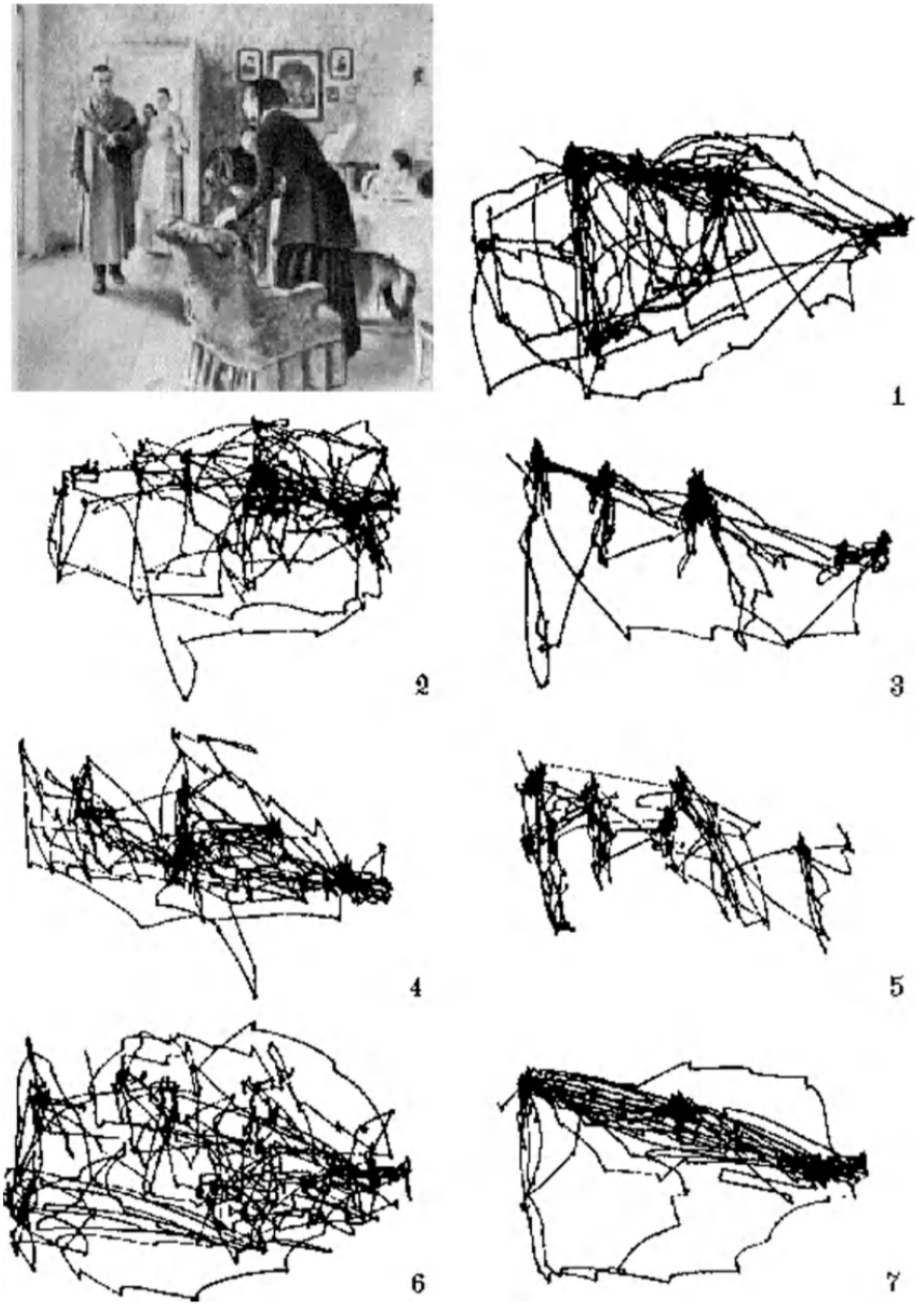

Figure 2.8: A sample of eye motion recordings. Each participant was presented the image shown in the top left. Each subject's eye motion as they observed the image was then recorded, demonstrating clear jumps between fixation points.

away. Vergence motion provides the smallest of the 3 displacement modes and is only present to provide changes in depth perception [32].

Up to 90% of time is spent with the eye in fixation [33] . During target fixation, the eye is continuously moving over a visual region corresponding to just

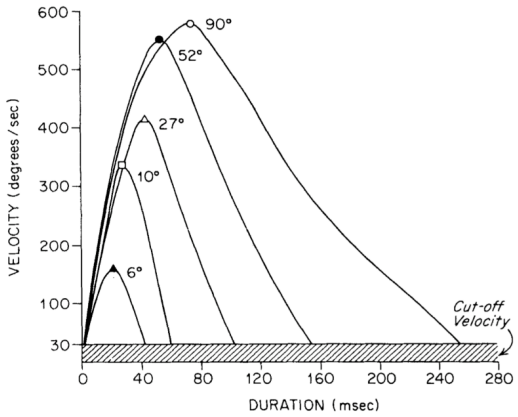

Figure 2.9: Velocity profiles for five different amplitude saccades in a normal subject.

50-150 micrometers [34]. Fixational eye motions are believed to perform two functions. First, it has been found that photoreceptors will filter out visual stimulus if it becomes stagnant, thus micro-motion of the eye acts to provide continuously changing visual stimulus [35]. Second, when the eye is held still during fixation, the ocular motor muscles may cause vision to drift over a small region, with a superimposed noisy tremor, resulting in fixation target tracking error [36]. The corresponding micro saccades act as an error correction mechanism, realigning the object of interest with the fovea.

The human eye tends to perform both voluntary and involuntary eyelid blinks during fixation periods, such that the focus of the visual field remains constant through the blink. However, eccentricity from initial gaze to resulting gaze after a blink can be as high as 15° [37]. In [38], it was found that spontaneous blinks have an average duration of (334 ± 67) ms, while voluntary blinks had a shorter total duration of (275 ± 37) ms. It was also found that the relative position of the eye had no relationship to the duration of the blink events.

2.3.3 Tracking of visual gaze

Eye tracking applications require an understanding of how the human visual system perceives the environment and transfers relevant information into any decision-making process. Depending on the application, certain elements of the eye-gaze tracking system require more sophistication than others. As such, it is useful to divide eye and gaze based tracking applications into four broad categories, as follows [39]:

Diagnostic Tracking: Off line measurement, assessment of a pre-recorded activity where gaze information of a subject was captured.

Active Tracking: Selection using the real-time gaze target of the subject as an input into a digital system, where the intent of the user is thought of much like a computer mouse input.

Passive Tracking: Foveated rendering, gaze contingent, where the measurement of the current gaze state results in a change in state corresponding to the gaze. A natural example is augmented reality where the current gaze must be matched by a shift in the layered virtual environment.

Expressive Tracking: Synthesis of representative gaze with action or state changes. E.g. to provide an avatar in a virtual reality environment with the users natural gaze, much like a reflection in a mirror.

Retinal eye implants fall under the passive tracking category, since their function requires that the current eye position is aligned with the target of the visual field scene being captured by the frame mounted camera. For these systems, the gaze tracking system design priorities align with other passive tracking systems, such as augmented reality systems. For patients in clinical trials of the Argus II, misalignment between the camera scene axis and the intended visual scene, based on the current eye state would results in discomfort, disorientation and nausea [6]. To reduce the negative effect of camera-eye misalignment, a passive gaze tracking system was implemented in [40] to allow for combined eye-head scanning of the environment. To determine the next intended point of interest for the camera to focus on, the current eye state provided by a passive eye tracker was combined with the current camera focus location within a closed loop feedback system. For the proposed Diamond Eye wireless power delivery system, a similar passive eye tracking methodology is implemented to ensure consistent power delivery by laser beam to the implant, to enable the patient with the freedom to move their eye about the visual field, unrestricted. The implementation of the passive eye tracking application is described in Chapter 3.

Chapter 3

Predictive Eye Implant Tracking for Power Delivery

3.1 Problem formulation - wireless implant tracking

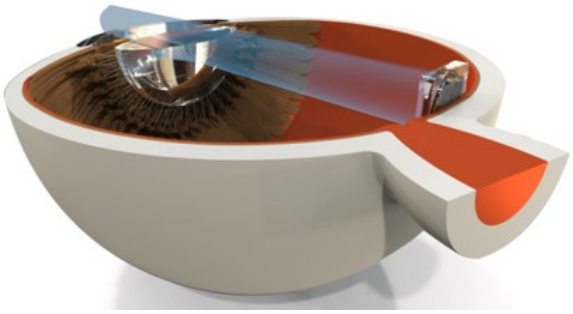

Figure 3.1: Render of a section view of the Diamond Eye implant embedded to the foveal region of the retina. A laser beam is shown entering through the pupil opening, targeting the implant. (Courtesy iBIONICS).

The Diamond Eye wireless retina implant (here on referred to as the wireless implant, or implant) is unique for it receives power and scene data by a modulated laser beam that targets a photo voltaic cell and a set of photo diodes integrated to the package. The implant itself is embedded to the retina, above the the foveal region where the visual cells have the highest density. A render of the implant position within the eye globe is provided in Figure 3.1. No other electronic elements or permanent eye wall incision is required. The implant package has a surface area of approximately 5 mm by 5 mm. In comparison to other retinal implants reviewed in Section 2.2.1, the wireless implant is the smallest, least invasive visual prosthesis surgical solution currently in development [41]. Figure 3.2 shows a sim-

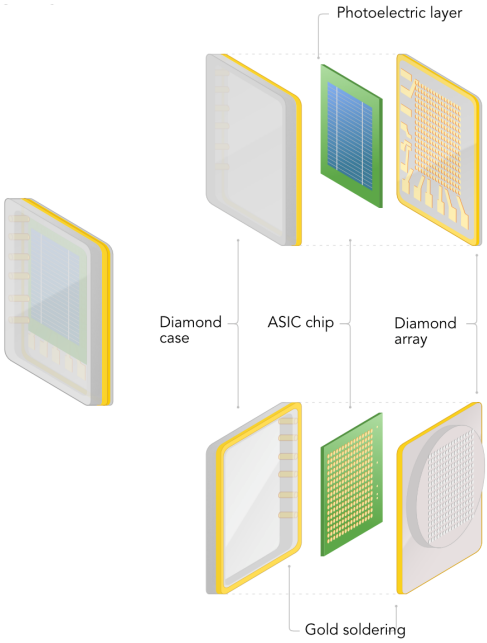

Figure 3.2: Schematic diagram of the structure of the Diamond Eye wireless retinal implant, enclosed within a diamond package. (Diagram courtesy of iBIONICS).

ple exploded diagram of the wireless implant. Figure 3.3 shows a prototype of the implant [41].

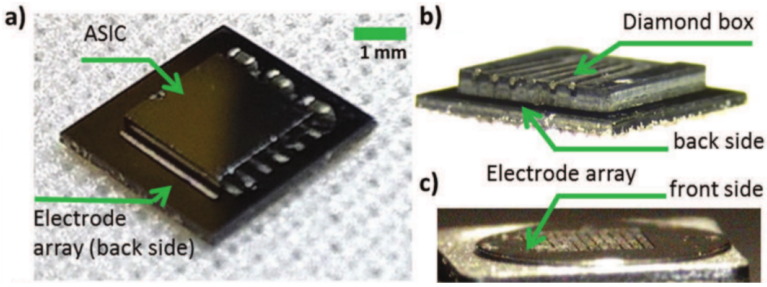

Figure 3.3: Electronic package of prototype implant. a) Partially assembled device, with ASIC visible. b) Diamond box containing electronics and electrodes. c) Shaved diamond box, with visible electrodes.

The primary focus of the work was to validate whether a directed laser beam based wireless power and data transmission system would be feasible to maintain the energy needs of the Diamond Eye implant during electrode stimulation. The partner company provided the idea of a directed laser beam that would both supply power and transmit visual scene information to the implant, and consistently target a photo voltaic (PV) cell mounted to the wireless implant. A study was provided that demonstrated that heating of the retinal implant and surrounding eye

tissue would be safely dissipated without causing harm to the patient [42]. The laser beam must continue to target the PV cell even as the implant recipient moves their eye about or interrupts tracking with normal eye blinks. The problem was presented with the explicit understanding that a laser beam was capable of providing a minimum threshold of 5 mW of power used to stimulate the electrodes of the implant while embedded in the eye. In the event of a complete loss of laser power, a set of capacitors on the implant would provide enough power to maintain a low power mode for approximately 400 milliseconds. Hence, the research question was formulated as an eye implant tracking problem.

iBIONICS highlighted several concerns over the viability of consistently powering the implant with a laser beam, such that electrode stimulation is maintained. First, the laser beam must provide sufficient power delivery when on target, i.e. the beam path intersects both the pupil opening, and the PV cell. iBIONICS have provided several nominal power requirements for the current implant prototype:

- The PV cell must be consistently supplied with at minimum 5 mW of power from the the PV cell to ensure full operation and stimulation of the electrode array.
- The beam width of the laser must be around 1.5 mm to ensure that in the event where the laser center falls off the PV cell, laser intensity distribution prevents a sudden loss of power while the patient's eye is open.

The tracking of the implant must be maintained as the patient looks around their visual scene with their eye. Therefore, the impact of eye motion modes on tracking must be considered:

- The characteristics of eye saccades must be considered for tracking. Saccades have a maximum speed of $700^\circ/s$, an average duration of 20-100 ms and cause a maximum eye globe angular displacement of 45° [26].
- Micro-motions of the eye during fixation may result in tracking jitter and error drift [34]. The time constant and spatial range of micro-motions must be accounted for by the control system for the laser tracking system.

The laser beam must successfully re-target the implant in the event of sustained loss of the target. Losses occur regularly due to eyelid blinks and drastic misalignment of the glass frame laser apparatus. Specifics about this aspect are:

- Blinks have an effective maximum duration of 300 ms [38].
- iBIONICS have provided that the capacitors of the implant allow for a low power mode, where the implant remains online but no stimulation occurs, with a discharge duration of 440 ms.

Finally, the laser tracking system must be designed with the constraint that it is wearable on the patients head without being uncomfortable or unwieldy. Therefore, the components of the laser directing system must be small and light weight such that their inclusion does not significantly increase the total weight of the glasses frame. iBIONICS supplied Figure 3.4 as a concept for the desired appearance of the first commercial prototype frame system.

Figure 3.4: Render of iBIONICS Diamond Eye Frame System concept (Courtesy of iBIONICS).

3.2 Proposed solution: Control of MEMS mirror for laser redirection, with camera acquisition of eye position

The current proposed architecture for the powering and data transmission system is comprised of a glasses frame mounted laser beam redirection system that utilizes a micro-electro-mechanical system (MEMS) mirror and a reflective glasses lens to direct the laser beam to the implant [43]. Figure 3.5 displays a close up view of a 1 mm diameter MEMS mirror surface, at a tilt angle that differs from its housing [44].

MEMS mirrors are small, millimeter scale devices that finely control the planar tilt of a single-crystal silicon surface that is coated by a thin reflective layer. MEMS mirror systems are central components found in environment beam scanning apparatus, and are used widely for several applications, such as machine perception,

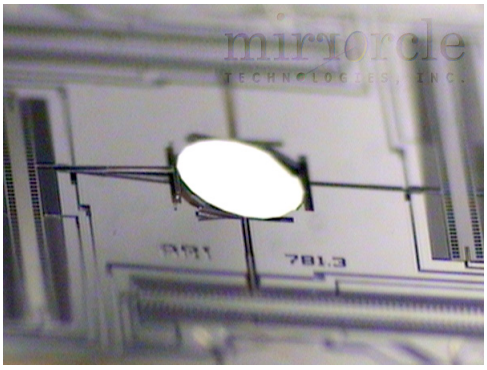

Figure 3.5: Macro photograph of a MEMS Mirror, Mirrorcle Technologies.

virtual or mixed reality, and autonomous vehicle sensing [45, 46, 47]. Micro-scale forces provided by mechanisms such as piezo-electric contractions act on the mirror gimbals to rapidly manipulate thef tilt angle. MEMS mirrors operated in a closed loop PID control for the purpose of tracking a desired tilt angle have been shown to achieve bandwidths as high as 1.5 kHz with negligible tracking error [48]. MEMS mirror's have a typical tilt range of $\pm 10°$, which can be further augmented through use of a small wide-angle projection lens. The control of a MEMS mirror system is highly repeatable due to the direct relationship between voltage applied and the corresponding tilt angle of the mirror itself, within less than a millidegree of error. Within the frame mounted laser direction system, a MEMS mirror will be the component used to control the angle of incidence of the laser beam through the pupil opening, onto the implant. Figure 3.6 provides a render of the experimental implant tracking laser redirection system's layout.

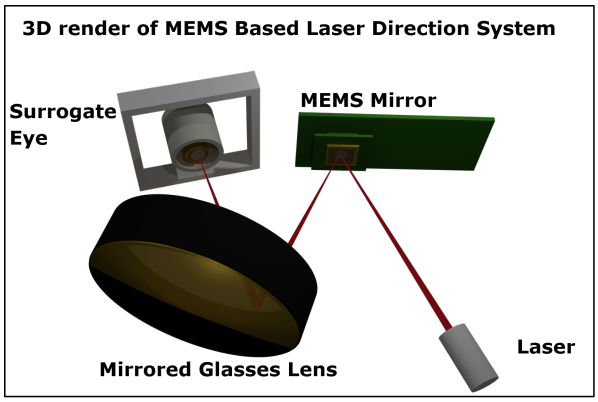

Figure 3.6: Render of the MEMS mirror system directing the laser beam into the surrogate eye. (courtesy Ross Cheriton).

The authors from [48] provide a simple second order dynamic plant model to

characterize the transfer function of the mirror angle $p(t)$ as a function of the voltage input V_{diff}. For the Mirrocle A3I12.2 MEMS 1.2 mm diameter mirror system (the same MEMS mirror used for the experimental system in Section 3.6), the relationship between control voltage signal and the resulting mirror angle is given by the transfer function:

$$\frac{p(t)}{V_{\text{diff}}} = K\frac{{\omega_n}^2}{s^2 + 2\zeta\omega_n + {\omega_n}^2} = 0.0486\frac{(16567\frac{rad}{s})^2}{s^2 + 2 \cdot 0.067 \cdot 16567\frac{rad}{s} + (16567\frac{rad}{s})^2} \quad (3.1)$$

where K is the combined voltage to angle gain constant for the mirror system, ζ is the mirror's damping ratio, ω_n is the mirror's undamped natural frequency, and s is the Laplace domain complex frequency variable.

With the addition of a low pass filter element, the Mirrocle A3I12.2 MEMS 1.2 mm diameter mirror system is able to sample any new tilt angle positions across its total tilt range within a 1 ms interval [49]. When combined with the reflective glasses lens, the MEMS mirror system is capable of continuously directing the laser to the implant, regardless of the eye's gaze position as the implant recipient moves their eye to view their surroundings.

A camera-based eye tracking method is used to provide current eye pupil position as feedback to the MEMS mirror implant tracking system. Given that the relationship between the location of the PV cell of the implant to the center of the pupil is constant, the pupil location of the patient may be used as the target for the laser redirection system. The flow of control signals for the MEMS mirror implant tracking system is shown with Figure 3.7.

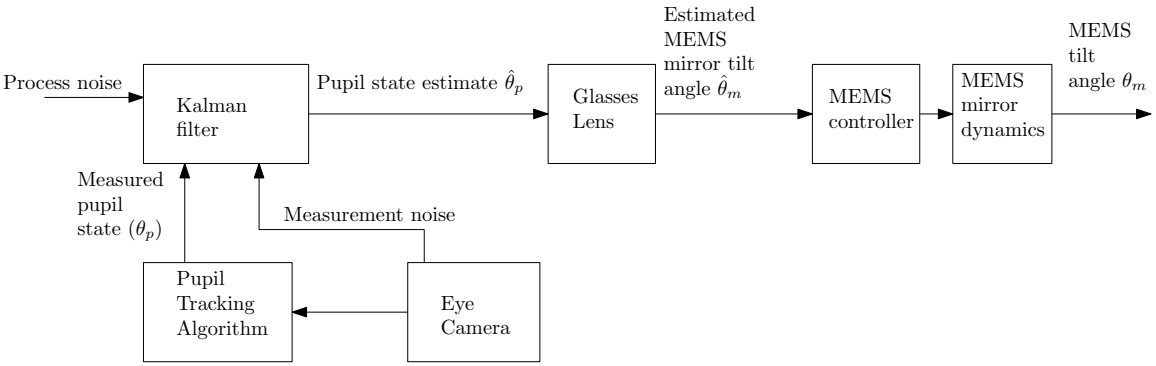

Figure 3.7: Simplified predictive implant tracking control block diagram.

The difficulty in camera-based eye tracking lies in the computer processing required, and the associated delay time. Any significant delay in the pupil position measurement will cause the resulting MEMS mirror laser position to lag the true

position of the implant. However, there is an upper limit to the amount of processing power that may be used to resolve the pupil position, due to the requirement that the eye tracking computer processing is done by a mobile computer unit with limited power reserves. In Appendix C.1, the proposed method to capture the implant position is described in detail. The practical implementation of a predictive implant tracking algorithm, based on the Kalman Filter algorithm is presented in Section 3.3. The Kalman Filter provides the MEMS mirror control system with a means to account for the expected measurement interval delays and associated angular eye drift errors due to usage of the camera based eye tracking scheme.

3.3 Predictive implant tracking with a Kalman Filter

The Kalman Filter is a recursive optimal estimator algorithm that estimates the next state (i.e. predicts the future state) of a dynamic system by combining information from a state-transition model, previous observations of state variables, and the characterization of statistical noise errors [50]. The Kalman Filter incorporates measurements to propagate in time the state estimate based on a prediction determined by the state transition model, and on information coming from measurements (when available.) Here we consider a standard discrete time setting, with time interval between two updated that must be greater than 1 ms, to ensure that the MEMS mirror has settled at its current directed position.

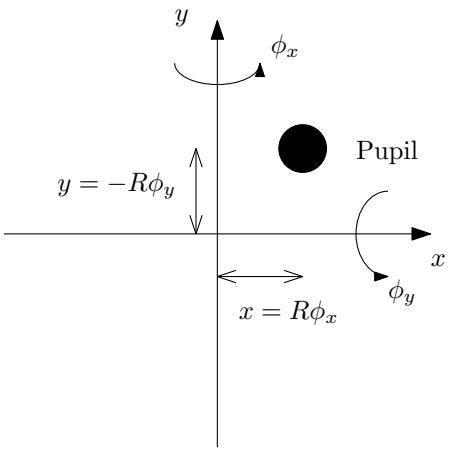

Figure 3.8: Simple illustration to show the convention used for pupil representation in a two-dimensional Cartesian coordinate system, where ϕ_x represents 'left-right' rotations, and ϕ_y represents 'up-down' rotations. R is the generic 2D rotation matrix that maps the Cartesian coordinates to the rotation angles.

The state-transition model adopted for the pupil's motion is a discrete time

stochastic process in which the state includes Cartesian position and velocity in a plane that is the projection of the region of the eye bulb relevant for the motion, and the acceleration, acting as the driving excitation, is distributed as Gaussian with zero mean and given standard deviations (along the two directions,) with parameters informed by the pupil's motion [51]. Specifically, let $\mathbf{p}(t)$ be the pupil's Cartesian position with velocity $\mathbf{v}(t)$, both vectors being two-dimensional to include the planar components in a global Cartesian frame, see Figure 3.8, where the origin of the Cartesian frame is placed to coincide with the intersection of the "straight-ahead" line of sight and the plane onto which the pupil's motion is projected. For deviations from the origin relatively small as compared to eye ball radius R, distortions introduced by the projection onto the plane are small; for large deviations, distortions should be properly accounted for. In reference to the eye globe motion, the PV cell is mounted directly below the pupil, hence moves with the pupil and the eye rotates as shown in Figure 3.1. Let the integer $k = 1, 2, \ldots$ label the time instants t_k at which updates occurr, and let $\Delta t_k = t_{k+1} - t_k$ be the update time interval. The discrete set of equations decribing the motion of an accelerated kinematic particle can be written as

$$\mathbf{p}_{k+1} = \mathbf{p}_k + \mathbf{v}_k \Delta t_k + \mathbf{a}_k \frac{\Delta t_k^2}{2} \tag{3.2}$$

$$\mathbf{v}_{k+1} = \mathbf{v}_k + \mathbf{a}_k \Delta t_k \tag{3.3}$$

where the two-dimensional vector $\mathbf{a}_k$ represents the pupil's acceleration at time t_k. Subscript k in the context of discrete time evolution means that the function is evaluated at time t_k. The acceleration describes the switching of the pupil motion from a fixation point to an eye saccade and is modelled as a white noise with standard deviation $1000^\circ/s^2$. The magnitude of the standard deviation corresponds to that of real eye motion [26].

The four dimensional state vector $\mathbf{x}_k$ is defined as

$$\mathbf{x}_k = \begin{pmatrix} \mathbf{p}_k \\ \mathbf{v}_k \end{pmatrix} = \begin{pmatrix} p_{xk} \\ p_{yk} \\ v_{xk} \\ v_{yk} \end{pmatrix} \tag{3.4}$$

where the subscripts x and y indicate the Cartesian direction of motion in 2D corresponding to the state vector element. The resulting state space representation

for the evolution of the motion of the pupil center is represented by the matrix equation:

$$\mathbf{x}_{k+1} = \mathbf{F}_k \mathbf{x}_k + \mathbf{G}_k \mathbf{a}_k \tag{3.5}$$

$$\mathbf{F}_k = \begin{pmatrix} 1 & 0 & \Delta t_k & 0 \\ 0 & 1 & 0 & \Delta t_k \\ 0 & 0 & 1 & 0 \\ 0 & 0 & 0 & 1 \end{pmatrix} \tag{3.6}$$

$$\mathbf{G}_k = \Delta t_k \begin{pmatrix} \frac{\Delta t_k}{2} & 0 \\ 0 & \frac{\Delta t_k}{2} \\ 1 & 0 \\ 0 & 1 \end{pmatrix} \tag{3.7}$$

where $\mathbf{F}_k$ and $\mathbf{G}_k$ are respectively the state transition matrix and the noise matrix, which propagates the linear motion of the pupil between time steps.

Measurements $\mathbf{z}_k$ of pupil center by the camera measurement system at time step k is given by the equation:

$$\mathbf{z}_k = \begin{bmatrix} 1 & 0 & 0 & 0 \\ 0 & 1 & 0 & 0 \end{bmatrix} \mathbf{x}_k + \mathbf{e}_k = \mathbf{H}\mathbf{x}_k + \mathbf{e}_k \tag{3.8}$$

where $\mathbf{H}$ is the observation matrix, and the vector $\mathbf{e}_k$ corresponds to the two dimensional Cartesian error associated with the camera measurements. It is important to note that the system model is based on a four dimensional state which includes position and velocity, whereas the camera measurements are limited to positions alone.

First, the Kalman filter generates a prediction, (notated by the subscript $k|k-1$), of the state vector at time step k along with the associated predicted error covariance matrix $\hat{\mathbf{P}}_{k|k-1}$

$$\hat{\mathbf{x}}_{k|k-1} = \mathbf{F}_k \hat{\mathbf{x}}_{k-1|k-1} \tag{3.9}$$

$$\hat{\mathbf{P}}_{k|k-1} = \mathbf{F}_k \hat{\mathbf{P}}_{k-1|k-1} \mathbf{F}_k^T + \mathbf{G}_k \mathbf{Q} \mathbf{G}_k^T \tag{3.10}$$

where the matrix $\mathbf{Q}$ is the 2×2 diagonal process noise covariance matrix, with nonzero entries quantifying process noise in the Cartesian plane where the pupil motion is projected and captured by the camera. If no measurement is available at time t_k, then the state estimate $\hat{\mathbf{x}}_{k|k-1}$ is used as the target position of the laser

beam, controlled by the MEMS mirror tilt angle.

If a measurement is made available at time t_k, the state estimate is corrected by accounting for the information provided by the measurement. The measurement residual $\mathbf{y}_k$ and associated covariance matrix $\mathbf{S}_k$ are

$$\mathbf{y}_k = \mathbf{z}_k - \mathbf{H}\hat{\mathbf{x}}_{k|k-1} \tag{3.11}$$

$$\mathbf{S}_k = \mathbf{R}_k + \mathbf{H}\hat{\mathbf{x}}_{k|k-1}\mathbf{H}^T \tag{3.12}$$

where $\mathbf{R}_k$ is the measurement error covariance matrix. $\mathbf{R}_k$ contains zero elements everywhere, except for the diagonal elements which represent the mean squared errors of the measurements.

The Kalman gain matrix $\mathbf{K}_k$ is calculated from the residual covariance matrix

$$\mathbf{K}_k = \mathbf{P}_{k|k-1}\mathbf{H}^T\mathbf{S}_k^{-1} \tag{3.13}$$

and it is then used to update the state estimate, denoted by the subscript $k|k$:

$$\hat{\mathbf{x}}_{k|k} = \hat{\mathbf{x}}_{k|k-1} + \mathbf{K}_k\mathbf{y}_k \tag{3.14}$$

$$\hat{\mathbf{P}}_{k|k} = (\mathbf{I} - \mathbf{K}_k\mathbf{H})\hat{\mathbf{P}}_{k|k-1} \tag{3.15}$$

where $\mathbf{I}$ is the identity matrix.

By incorporating the information provided by the available measurement, the previous state estimate, the measurement error, and the process noise, the Kalman filter produces updated state estimates that are improved over measurements or estimates of the state variables alone. A useful graphical representation of the underlying Bayesian process in terms of intersection of two dimensional error ellipsoids associated to error covariances is shown in Figure 3.9 [52].

The Kalman filter allows for predictions of the current system state to be made during time steps where no measurement is available. The ability to make predictions of the system state when no measurement is present is useful during periods where there is a missed measurement, or the lower frequency of measurements results in significant drift from the true position as the eye moves. The Kalman filter is also ideal in applications where any state estimate computation has little memory available and minimal computational overhead [53]. For the implant laser tracking application, the Kalman Filter meets both requirements. When speaking in terms of computational requirements, the Kalman Filter implementation used is simple. Only the previous state estimate is stored into memory, and the algorithm

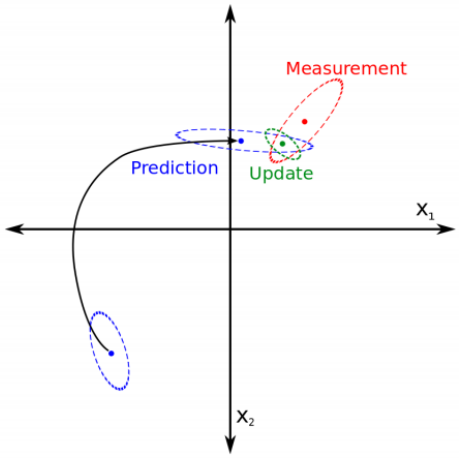

Figure 3.9: The combination of information about the measurement error covariance (represented by red ellipse) and the prediction error covariance (blue) by the Kalman Filter results in the updated reduced error covariance (green).

complexity is low due to the low dimension of the matrices involved, at most 4x4.

3.4 Simulation of implant tracking and power delivery

It is assumed that the wireless implant is embedded on the foveal region, directly beneath the center of the eye's pupil opening. The laser beam should intersect the pupil at a perpendicular angle to ensure that the laser beams targets the center of the PV cell for optimal power delivery. To determine the necessary orientation for the MEMS mirror to be driven to, to redirect the laser to the implant, the system must quickly and accurately determine the pupil center coordinates on the eye globe. The treatment of the glasses frame system becoming misaligned from the calibrated system, resulting in the pupil occluding the PV cell are considered in Chapter 4.

A MATLAB simulation was prepared with the intent of validating the effectiveness of the MEMS mirror controlled implant tracking solution. Real eye motion data, provided by R. Cheriton, was generated by the method described in Appendix C.1. The eye motion data provides realism to the simulated environment. The MATLAB simulation program can be found in Appendix C.2.

As the eye moves about, a calculation of the power received by the implant

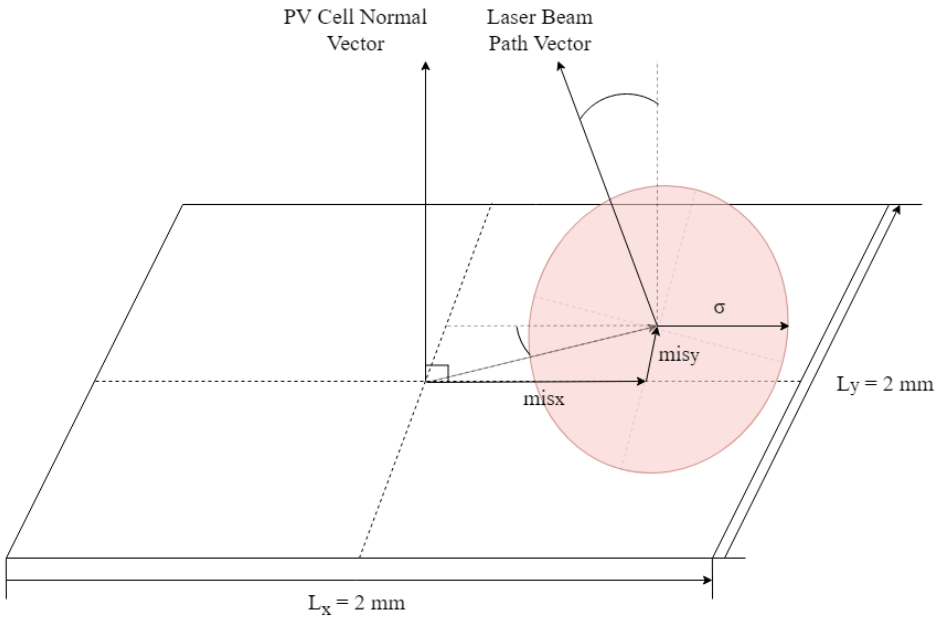

Figure 3.10: Illustration of the misaligned laser beam with beam width σ intersecting the PV cell of the implant. L_x and L_y represent the PV cell side lengths. The resulting misalignment vector components of the laser beam center to the PV cell center are indicated by mis_x and mis_y.

from the laser beam is performed. The power calculation incorporates the motion of the eye, the beam width and intensity of the laser, the surface area of the PV cell mounted to the implant, and the beam path of the laser that results from the state of the MEMS mirror. Figure 3.10 illustrates an example of a misaligned laser beam intersecting the PV cell. A description of the laser beam power distribution, and the calculation for the beam width can be found in Appendix A.

The simulation occurs in discrete time at the rate 240 Hz, set to be twice the eye tracking camera measurement rate of 120 Hz. Each discrete time step k is spaced by an interval of 4.2 ms. The spacing interval is selected such that for every time step, the MEMS mirror has reached a steady state position. The relative position of the laser beam center axis is compared to the position of the PV cell center. The difference between these two axes is described as the misalignment error, which is used to determine the amount of laser light that is incident on the PV cell. The human eye globe is assumed to have a diameter of 24 mm and a pupil size no smaller than 3 mm in direct sunlight conditions [54]. A simple illustration of the laser beam intersecting the pupil with slight misalignment is shown in Figure 3.11.

The wireless implant is embedded on the retina along the fovea, directly below the pupil opening of the eye. It is assumed that the MEMS mirror directs the

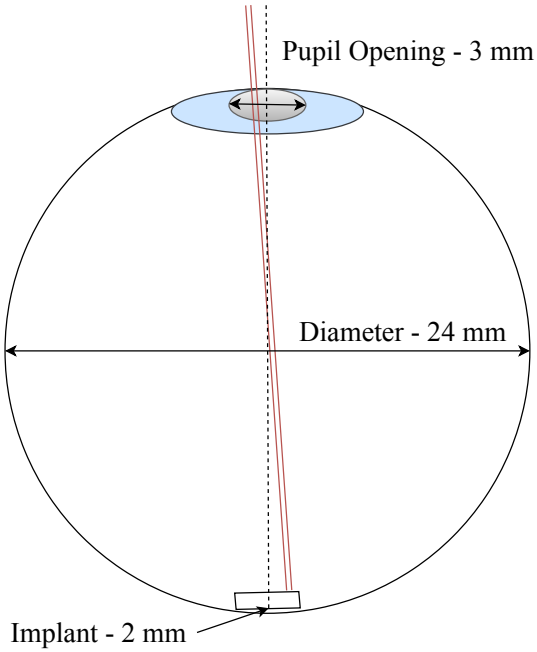

Figure 3.11: Illustration of the eye with size parameters used in the simulation environment. The laser is shown slightly misaligned from the normal angle of the pupil.

laser beam path to be coincident to the pupil opening at the normal angle. Since the PV cell is directly below the pupil opening, the laser beam intersects the PV cell perpendicularly. To ensure consistent power delivery during eye motion, the MEMS mirror must redirect the laser to match the eye motion, such that the laser misalignment is minimized.

To calculate the power received by the PV cell from the laser beam, the PV cell is discretized into a square grid of 100×100 elements. The two grid Cartesian directions are labelled by indices i and j. The incidence of the laser beam to the PV cell grid elements is checked. The amount of laser light power incident on grid element (i, j), denoted by $P_{(i,j)}$ is calculated by the expression:

$$P_{(i,j)} = I_{max} \exp \frac{-(i - \frac{L_x}{2} - mis_x)^2 - (j - \frac{L_y}{2} - mis_y)^2}{2\sigma^2} \tag{3.16}$$

where I_{max} is the maximum laser intensity at the center of the Gaussian beam. The beam width σ is defined by the full width at half maximum convention, as described within Appendix A.

The the total power received by the PV cell P_{total}, is calculated by summing the

power contribution for all grid elements that the laser beam is incident upon

$$P_{\text{total}} = \eta_{PV} \sum_{i}^{100} \sum_{j}^{100} P_{(i,j)} \tag{3.17}$$

where η_{PV} is the conversion efficiency of the PV cell from incident laser beam energy to the resulting output energy to the implant. The conversion efficiency of the PV cell was provided by iBIONICS to be 95%.

The method described in Appendix C.1 was used to capture real eye motion data to be used in the simulation. To test the Kalman filter algorithm, measurements in simulation are provided by corrupting with noise the real eye motion data, and the Kalman filter estimates are compared with the non-corrupted eye motion data to test the accuracy. Specifically, simulated camera measurements of the pupil coordinates are generated by adding measurement noise to the true eye motion data, with variance of $\pm 2.0^\circ$ (corresponding to a distance of $\pm$4.1mm for a 24mm diameter eye). Observations occur at an interval selected to match the experimental system camera frame rate. To capture the effect of processing delay, the MEMS mirror controller is provided the measurement one discrete time step later than when the measurement was taken. The 2D path of 10 discrete time step positions for the true pupil position, the Kalman filter generated predicted position, and the camera based measured position are shown in Figure 3.12.

3.5 Discussion of simulation results

The simulation was used to test different implant tracking scenarios by modifying simulation parameters of interest. Quantifying the performance of the implant tracking solution is of particular interest, as well as the scenarios where the improvement offered by the predictive tracking algorithm is worthwhile. The total power collected by the PV cell is used as the metric to characterized the effectiveness of the implant tracking for the given simulation parameters. Ultimately, the simulation allows for the investigation of system parameters and performance, which has already proved useful prior to the development of the experimental system described in Section 3.6.

In the first simulation with parameters described in Table 3.1, the pupil measurement camera is prescribed a framerate of 120 fps and measurement error of 2 mm. The simulation measures the amount of power received by the implant

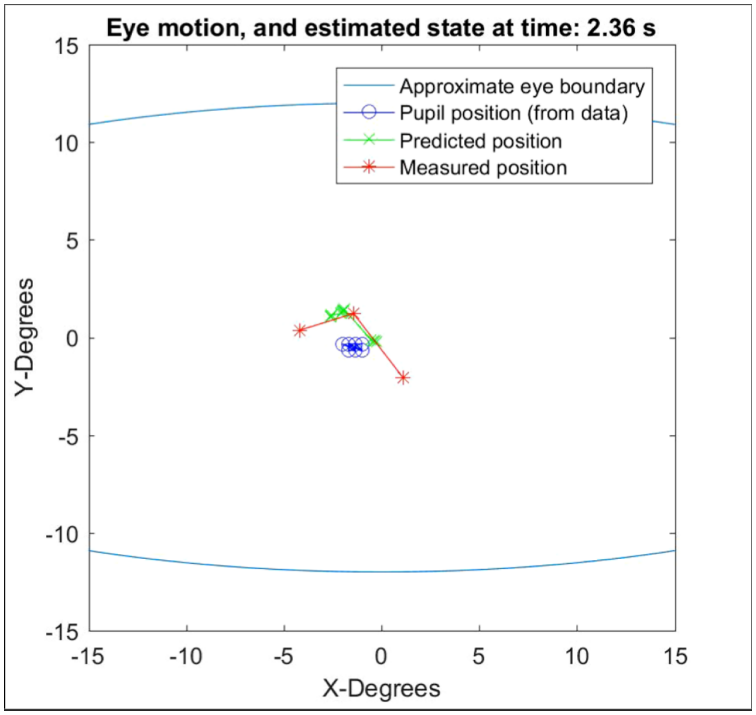

Figure 3.12: 10 discrete time steps of simulated true eye motion, measurement and state estimate position. Note how predicted state estimates (green cross) are closer to true position (blue circle) than noisy measurements (red star).

Parameter	Symbol	Value
Process noise	$\mathbf{a}_k$	$1000^\circ/s^2(208mm/s^2)$
Measurement noise covariance matrix	$\mathbf{R}_k$	$\begin{bmatrix} 2^\circ & 0 \\ 0 & 2^\circ \end{bmatrix}$
Laser beam width	σ	1.5 mm
Simulation interval rate	$\frac{1}{\Delta t}$	240 Hz
Observation sampling rate	$\frac{1}{\Delta t_{meas}}$	120 Hz
PV cell square boundary length	L	2 mm
Laser beam maximum intensity	I_{max}	$2.55\frac{mW}{mm^2}$
PV cell conversion efficiency	η_{PV}	95%

Table 3.1: Parameters for the first simulation, with a higher performance pupil tracking camera.

from the laser beam, where the amount of power received depends on the implant tracking performance. If the laser beam falls off of the PV cell during the simulation due to either eye motion or the combined effect of incorrect state estimates and erroneous measurements, the total power received by the implant will drop. Some variation in power is expected, however in general the mean power deliv-

ered to the implant must exceed the 5 mW threshold provided by iBIONICS. For the representative eye motion data sample used within the simulations, the volunteer was instructed to simply gaze in different positions as normal. The eye motion sample data includes blink events, saccades, and periods of fixation on a target where fixational motions occurred.

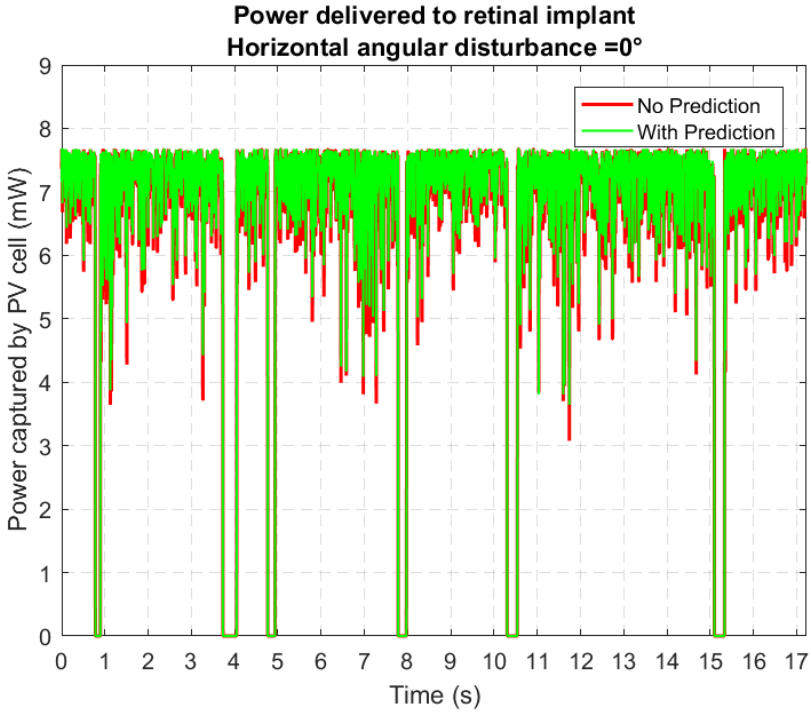

Figure 3.13: Power delivered to the implant with the simulation parameters in Table 3.1. The green power curve corresponds to implant tracking with the predictive algorithm. The red power curve corresponds to the measurement only approach to implant tracking.

Figure 3.13 displays two power curves over the same representative eye motion sample for two different control modes: through state estimate generated with the predictive tracking algorithm described in Section 3.3, and through measurement only where the MEMS mirror targets the most recent eye position measurement. It is important to note that extended drops in power to zero correspond to eye blink events, where the laser beam becomes blocked by the eyelid. Within the first simulation, the improvement for implant tracking provided by the predictive tracking algorithm is minimal, with a 2.2% improvement of of mean power delivered to the implant. With the predictive tracking algorithm, the mean power delivered is 7.19 +/- 0.65 mW, compared to measurement only where mean power delivered is 7.11 +/- 0.69 mW. Taking the difference of the two power curves, shown

in Figure 3.14, shows that beyond occasional state estimate errors, the predictive tracking algorithm consistently provides more power than the eye measurement only approach. The average difference in power over 440 ms (corresponding to the discharge time of the implant's capacitors) is useful in showing the trend of the power difference during the simulation.

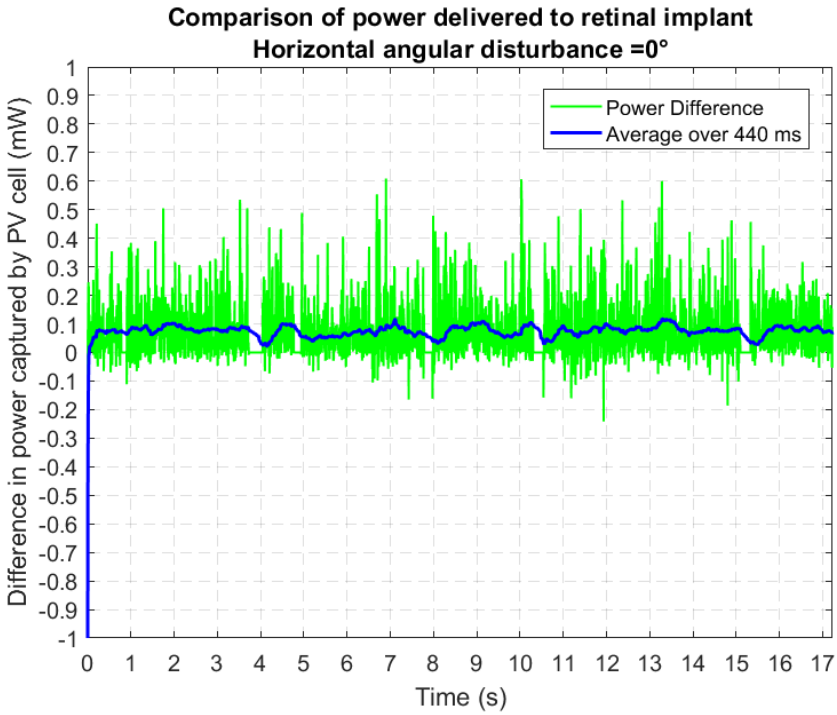

Figure 3.14: The difference of the two power curves for the simulation parameters in Table 3.1.

In the second simulation, a lower quality camera was considered by corrupting the true camera measurements with a higher noise than that present in the first simulation. Beyond the differences of the camera specifications with a 60 fps framerate and measurement error of 4 mm, the simulation parameters are set to the same as the first simulation, as shown in Table 3.2. The results of the second simulation, shown in Figure 3.15, show that the higher measurement error combined with the lower framerate results in a higher power variation than compared to the first simulation result, Figure 3.13. In particular, during saccades, the poor measurement results in the power dipping below the 5 mW threshold frequently. The mean power delivered to the implant is improved by 3.4%, with the predictive tracking algorithm mean power of 6.13 +/- 1.32 mW compared to the measurement only mean power of 5.92 +/- 1.44 mW. When considering the mean power standard deviation, it can be claimed that neither method is consistently above the

Parameter	Symbol	Value
Process noise (acceleration magnitude)	a_k	$1000^\circ/s^2$
Measurement noise covariance matrix	$\mathbf{R}_k$	$\begin{bmatrix} 4^\circ & 0 \\ 0 & 4^\circ \end{bmatrix}$
Laser beam width	σ	1.5 mm
Simulation interval rate	$\frac{1}{\Delta t}$	240 Hz
Observation sampling rate	$\frac{1}{\Delta t_{meas}}$	60 Hz
PV cell square boundary length	L	2 mm
Laser beam maximum intensity	I_{max}	$2.55 \frac{mW}{mm^2}$
PV cell conversion efficiency	η_{PV}	95%

Table 3.2: Parameters for the second simulation.

5 mW threshold. Note that the variation is reduced with the application of the Kalman filter.

By reviewing the difference of the two power curves for the second simulation, shown in Figure 3.16, it can be seen that the predictive tracking at certain time intervals exceeds the performance of the measurement only solution by as much as 1.1 mW. From examination of the second simulation results shown in figures 3.15 and 3.16, it is evident that advantage for using the predictive tracking algorithm is increased if the implant tracking is negatively affected by a lower quality camera measurement system.

To further investigate the effect of the camera parameters, additional results were obtained by setting all simulation environment parameters to be similar to the first and second simulations, and only varying the values of the measurement error and camera framerate. Performance comparison in terms of statistics of aggregate data (from time histories) is shown in Table 3.3.

The effect of increasing the camera measurement error results in a drastic increase of the standard deviation of power delivered, and a lower mean power delivered. The Kalman filter improves the power delivery to the implant, increasing mean power by 0.5%, 3.4%, 8.6% and 13.8% for measurement error of 2 mm, 4 mm , 6 mm and 8 mm respectively.

The decrease of the camera framerate results in the decay of the performance gain provided by using the predictive tracking algorithm, while increasing the variation of the mean power delivered to the implant. The Kalman filter offers a percentage improvement of 6%, 3.4%, 1.5% for frame-rates of 120 fps, 60 fps and 30 fps respectively. Notably, the Kalman filter causes the performance to be identical to measurement alone with a framerate of 15 fps. The decreasing power

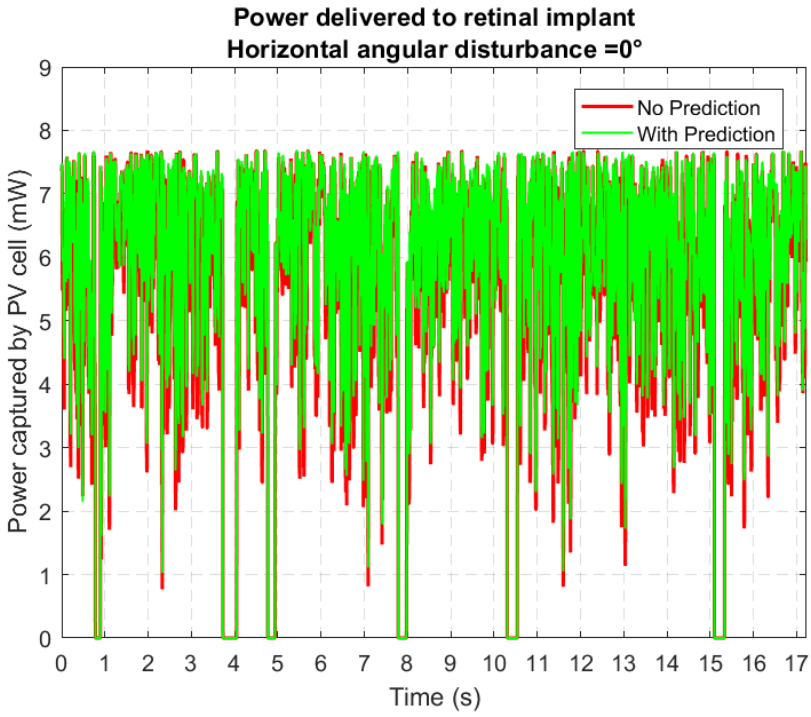

Figure 3.15: Power delivered to the implant for the simulation parameters in Table 3.2, with framerate of 60 fps. The green power curve corresponds to implant tracking with the predictive algorithm. The red power curve corresponds to the measurement only approach to implant tracking.

delivery advantage effect, as the camera framerate lowers, may be attributed to the state estimate confidence decreasing over successive algorithm iterations where no measurement update is provided. At 15 fps, there is a 67 ms delay between measurement updates, which exceeds the mean of a typical saccade duration by as much as two times [26]. Therefore, it can be argued that with the provided predictive tracking algorithm, the lower limit of the camera framerate is 30 fps. Above 30 fps, the eye motion is accurately modelled by a stochastic linear system, with eye acceleration treated as process noise. In line with the background theory for the Kalman filter, if the process noise and the state transition model of the eye motion are correctly characterized, and the measurement error is significant, the Kalman filter will produce state estimates that significantly improves upon measurements alone. [50, 53]. To conclude the discussion of the simulation results, within the validity defined by the conditions considered here, there is indication that with inclusion of the predictive tracking algorithm, a camera must have a frame rate greater than 30 fps to ensure that power delivered to the implant is consistently above the 5 mW threshold.

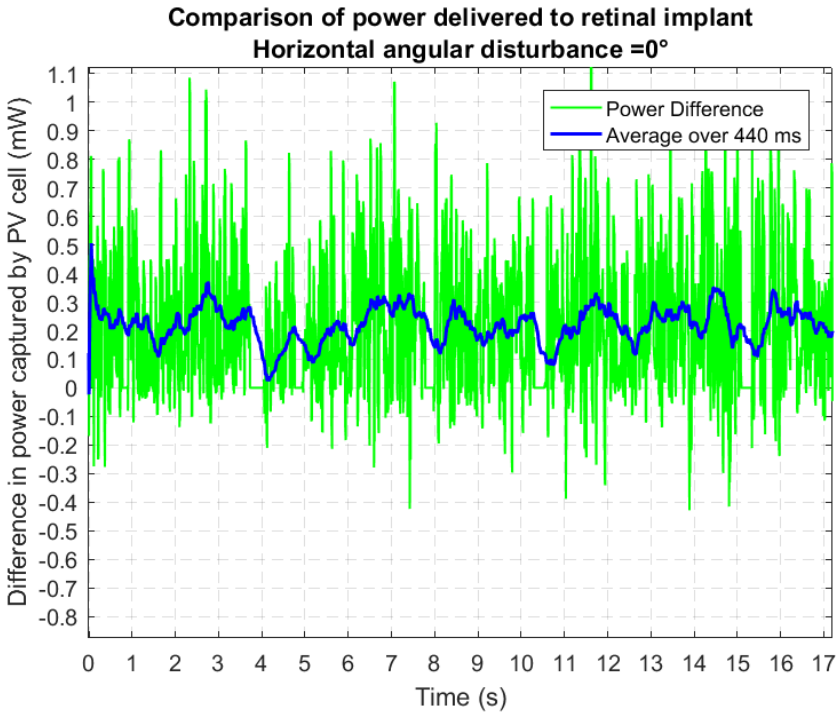

Figure 3.16: The difference of the two power curves for the simulation parameters in Table 3.2.

3.6 The experimental implant tracking system

In parallel to the work performed that is discussed within this document, an experimental prototype system was developed in parallel by a separate team, consisting of R. Cheriton, J. Cook, K. Vyas, and K. Hinzer, all members of the SUNLAB at the University of Ottawa. The hardware prototype system was developed in partnership with iBIONICS to present a proof of concept for a low cost implant tracking system to direct a laser beam to power a wireless retinal implant. The purpose of the prototype was to provide the University of Ottawa and iBIONICS to test the implant tracking system for several different system configurations, including different eye motion samples, eye tracking camera systems, optical arrangements, and computer hardware. The system had the developmental requirement that all components must be small, light weight and compact such that they could be mounted to a glasses frame. The experimental system provides a means for a user to characterize the performance of the implant tracking system configuration.

The experimental system consist of a surrogate eye, the MEMS mirror, a gold-coated reflective glasses lens, a low cost pupil tracking camera, and a LattePanda micro-PC board running Windows 10. A front view picture of the system looking

KF filter?	Measure err	Framerate	Mean +/- Std dev	% Improve
Yes	2 mm	60 fps	7.13 +/- 0.70 mW	0.5%
No	2 mm	60 fps	7.09 +/- 0.72 mW	–
Yes	4 mm	60 fps	6.13 +/- 1.32 mW	3.5%
No	4 mm	60 fps	5.92 +/- 1.44 mW	–
Yes	6 mm	60 fps	5.05 +/- 1.83 mW	9.3%
No	6 mm	60 fps	4.62 +/- 2.01 mW	–
Yes	8 mm	60 fps	4.19 +/- 2.17 mW	15.7%
No	8 mm	60 fps	3.62 +/- 2.27 mW	–
Yes	4 mm	120 fps	6.35 +/- 1.16 mW	6.5%
No	4 mm	120 fps	5.96 +/- 1.40 mW	–
Yes	4 mm	60 fps	6.13 +/- 1.32 mW	3.5%
No	4 mm	60 fps	5.92 +/- 1.44 mW	–
Yes	4 mm	30 fps	6.08 +/- 1.35 mW	1.5%
No	4 mm	30 fps	5.99 +/- 1.40 mW	–
Yes	4 mm	15 fps	5.80 +/- 1.59 mW	-0.3%
No	4 mm	15 fps	5.82 +/- 1.58 mW	–

Table 3.3: Comparison of mean and standard deviation of power delivered to implant during simulation, where the measurement error and camera framerate are varied.

into the surrogate eye is shown in Figure 3.17(a). A back, top-down view picture of the system showing the laser beam path is shown in Figure 3.17(b).

- The surrogate eye is rotated by a pair of servo motors to simulate the motion of a real eye, and is provided power and eye rotation coordinates by its own Raspberry Pi board. The surrogate eye follows a sample of real eye motion data to imitate the motion of a real eye.
- A lens shaped like a pupil lens is mounted at the opening of the surrogate eye.
- A quadrant photo diode (QPD) that is used to capture the location of the laser beam center is mounted at the back of the surrogate eye. The QPD is mounted in a similar location to where the PV cell would be for the real implant in a real eye, and therefore can be treated as the experimental analogue to the wireless implant. Hence, the position of the laser beam relative to the center of the QPD is treated as the implant tracking error during the experiments.

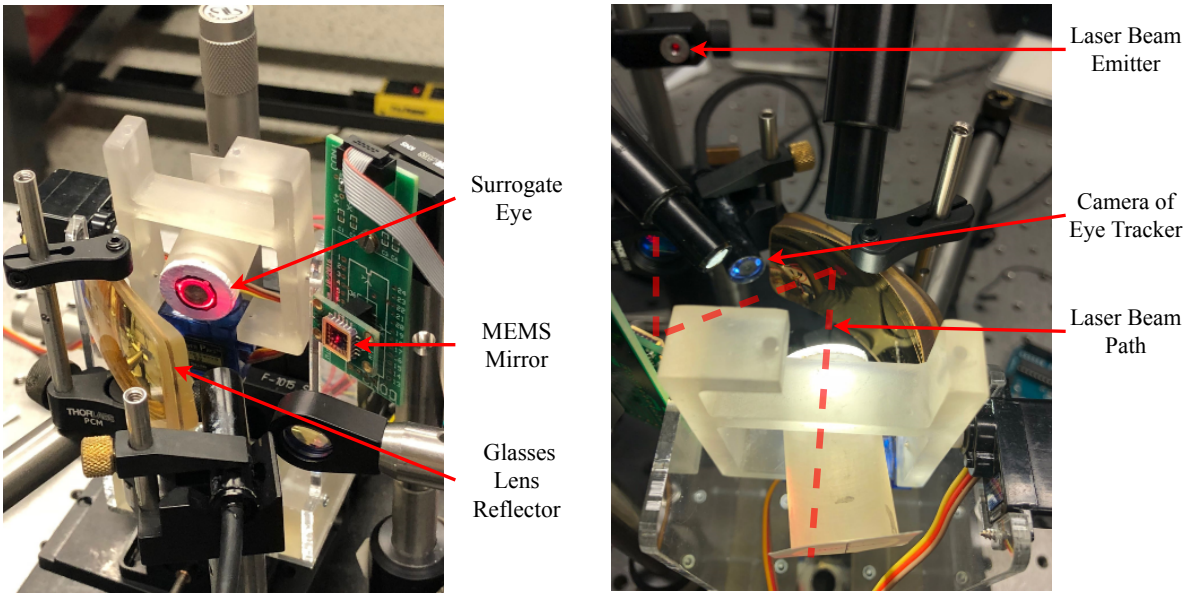

(a) (b)

Figure 3.17: Picture of the experimental system, showing (a) the three main components: the surrogate eye, the MEMS mirror, and the glasses lens reflector; and (b) the optical path of the laser beam, with the laser emitter visible in the background.

- The Mirrocle A3I12.2 MEMS 1.2 mm diameter mirror system includes its own controller, which reads coordinates provided by the implant tracking controller on the LattePanda.
- The gold-coated reflective glasses lens has an ellipsoidal geometry. This geometry ensures that the laser beam reflects at a predictable angle into the eye implant. This feature is described further within Section 4.1.
- The low cost pupil tracking camera provides the measured eye coordinates through a pupil edge detection algorithm provided by the OpenCV library. The camera takes pictures of the eye at a rate of 60 fps. The camera eye position measurement system was found to have an estimated measurement error of +/- 2°. The delay time before a measurement is made available was found to be approximately 20 ms.
- The LattePanda acts to supply MEMS mirror coordinates through an implant tracking controller developed within C++. The C++ program implements the predictive tracking algorithm described within Section 3.3. It is provided measurements by the the pupil tracking camera feedback.

It was found that with the predictive tracking algorithm enabled, the eye po-

sition estimates contributed to higher performance implant tracking. The results from one representative experiment is shown in Figure 3.18, where the misalignment error of the laser beam center relative to the QPD over time is shown by two clusters. With the Kalman filter enabled, the misalignment error was bounded to 2 mm in the X-axis, and 1 mm in the Y-axis. For the same motion sample without the Kalman filter enabled, the misalignment error increased to 4 mm in the X-axis, and 2 mm in the Y-axis, an increase of 100%. Similar to the simulated experiments, the real experimental prototype demonstrates that the predictive tracking algorithm helps in augmenting the performance of the MEMS mirror and camera based eye tracking system, through compensation of the measurement error and measurement update delays.

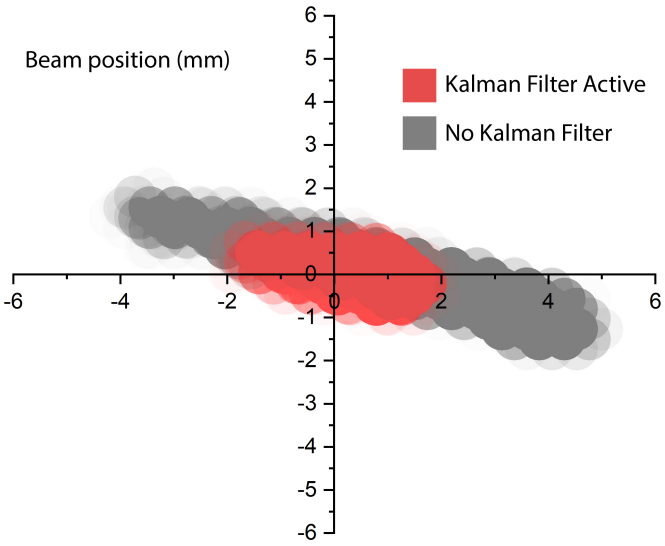

Figure 3.18: Qualitative result of laser beam center misalignment measured by the QPD for a representative real eye motion sample. With the Kalman filter enabled (red), the laser beam is clustered closer to the center of the QPD than compared to where the Kalman filter is not active (grey).

Chapter 4

Misalignment Compensation via Laser Retargeting

4.1 Reflective lens geometry and modeling

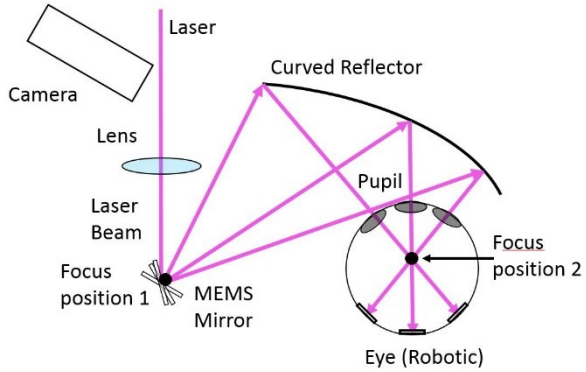

Figure 4.1: The pink line indicates different paths of the laser beam depending on the angle of the MEMS mirror and eye rotation. Deflection in only one dimension is shown, however deflection can occur in two dimensions.

The implant tracking by pupil tracking solution presented in Chapter 3 hinges on the optical property of an ellipsoidal reflector. For any mirrored ellipses (a cross section of the ellipsoid), if the source of a beam of light is coincident with one focus of the ellipse and reflects off the inwards curved surface, the light is always reflected to the second focus of the same ellipse. With the laser redirection system, the default frame position is oriented such that the MEMS mirror and the center of the eyeball are placed at the two foci of the glasses reflective ellipsoidal lens. When the mirrored glasses frame is held in the default position on the patients

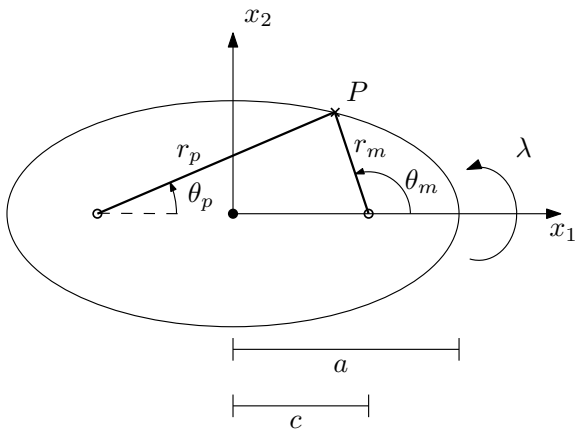

Figure 4.2: Schematics of an ellipse with relevant geometric parameters.

face, the laser beam path travels from the MEMS mirror position, reflects off of the ellipsoidal reflector lens, and into the center of the eye. This relationship is illustrated in Figure 4.1.

The geometry illustrated in Figure 4.2 shows the geometric path of a laser beam, emitted from one focal point, to the incident point, where the reflected beam travels to the second focal point. The coordinates of point P in the rectangular Cartesian system $\{x_1, x_2\}$ are

$$P \equiv (c + r_m \cos\theta_m, r_m \sin\theta_m) = \left(-c + r_p \cos\theta_p, r_p \sin\theta_p\right) \tag{4.1}$$

where a is the major radius length of the ellipse, c is the focal length, f_m and f_p are the focal points at the MEMS mirror and the eye center respectively, r_m and r_p form laser beam path sections reflected from point P on the ellipse, and θ_m and θ_p are the directions of the laser beam path from each focus. The 3D ellipsoidal-like shape of the reflector lens is obtained by revolving a segment of the 2D ellipse about the major axis, denoted by the rotation λ.

This equality, along with the fundamental relation $r_m + r_p = 2a$ gives the system of equations

$$r_p + r_m = 2a \tag{4.2a}$$

$$r_p \cos\theta_p - r_m \cos\theta_m = 2c \tag{4.2b}$$

$$r_p \sin\theta_p = r_m \sin\theta_m \tag{4.2c}$$

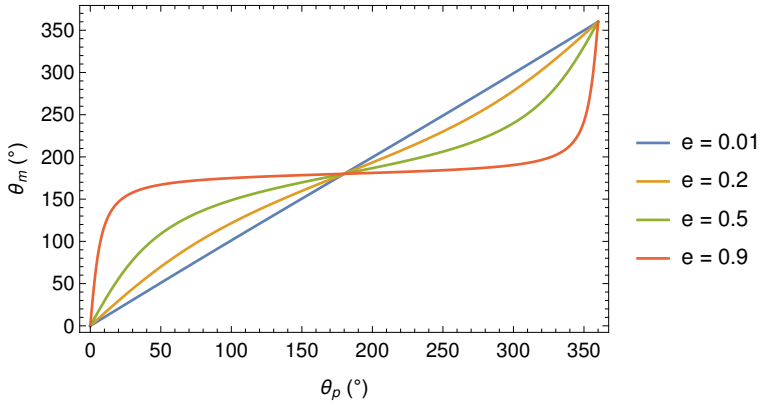

Figure 4.3: Numerical solutions of characteristic equation (4.4) for different eccentricities e.

By eliminating r_m and r_p the following relation is obtained

$$\sin\theta_m \cos\theta_p - \sin\theta_p \cos\theta_m - e\left(\sin\theta_m + \sin\theta_p\right) = 0 \tag{4.3}$$

where $e = \frac{c}{a} < 1$ is the eccentricity. After further simplification

$$\sin\left(\theta_m - \theta_p\right) - e\left(\sin\theta_m + \sin\theta_p\right) = 0 \tag{4.4}$$

Note that consistently with the geometry in Figure 4.2, the identity (4.4) is identically satisfied for $\theta_p = \theta_m = 0$ and $\theta_p = \theta_m = \pi$. Also, for $e = 0$ (circle), (4.4) it correctly predicts $\theta_m = \theta_p$.

Numerical solutions of the characteristic equation (4.4) are shown in Figure 4.3 for different eccentricities. For small eccentricity the solution $\theta_m(\theta_p)$ approaches a straight line with slope 1 (circle). When $e \to 1$, the ellipse degenerates to a line, with corresponding binary solution.

The glasses frame laser redirection system takes advantage of the reflector lens optical properties by manufacturing the frame such that the implant, within the eye, rotates about one focal point, and the MEMS mirror is placed at the other. The eye globe is approximated by a sphere of radius R_p centered at $(-c, 0, 0)$ in the system of rectangular Cartesian coordinates $\{x_1, x_2, x_3\}$. By considering the change to spherical coordinates $(R_p, \lambda, \theta_p) \mapsto (x_1, x_2, x_3)$

$$\begin{cases} x_2 = R_p \sin\lambda \cos\theta_p \\ x_3 = R_p \sin\lambda \sin\theta_p \\ x_1 = R_p \cos\lambda \end{cases} \tag{4.5}$$

the pupil can be described as a point in a three dimensional space with coordinates (R_p, λ, θ_p), where λ is the longitude and θ_p is the co-latitude of the spherical coordinates system. Considering the reflective lens to be an ellipsoid of revolution with x_1 as axis of symmetry, the state of the MEMS mirror is trivially described by the set of spherical coordinates (λ, θ_m) centred at $(c, 0, 0)$.

Note that the geometric construct described here assumes that the pupil's "zero" position is pointing towards the MEMS mirror ($\theta_p = 0$), and the MEMS mirror rest position is pointing away from the pupil ($\theta_m = 0$). If one wants to modify the configuration so that at rest both the mirror and the pupil point toward the lens, it is sufficient to introduce the variables

$$\tilde{\theta}_p = \theta_p - \frac{\pi}{2}$$
$$\tilde{\theta}_m = \theta_m - \frac{\pi}{2}$$

Upon substitution, the characteristic equation (4.4) becomes

$$\sin\left(\tilde{\theta}_m - \tilde{\theta}_p\right) - e\left(\cos\tilde{\theta}_p + \cos\tilde{\theta}_m\right) = 0 \tag{4.6}$$

4.2 Glasses frame motion and laser misalignment

This section is dedicated to the frame disturbance problem. Consider the simplified geometry in Figure 4.4. In the global reference system centered at the nose pad of the glasses frame, O_L, F_m and F_p represent the center and the two foci of the elliptical lens respectively. In the reference frame in Figure 4.2, the position vectors for these points are

$$\mathbf{r}_{O_L} = x_{O_L}\mathbf{e}_1 + y_{O_L}\mathbf{e}_2 \tag{4.7a}$$
$$\mathbf{r}_{F_m} = \mathbf{r}_{O_L} + c\mathbf{e}_1 \tag{4.7b}$$
$$\mathbf{r}_{F_p} = \mathbf{r}_{O_L} - c\mathbf{e}_1 \tag{4.7c}$$

where c is the focal distance from the center of the ellipse, and $\mathbf{e}_1$ and $\mathbf{e}_2$ are unit vectors along the coordinate axes.

Consider now a rotation θ around the axis perpendicular to the plane in Figure 4.5, passing by the origin. This disturbance is due to a rigid body disturbance of the glasses frame, moving the frame away from its original position. The rotated glasses lens is schematized in Figure 4.5, where the new rotated points are labelled

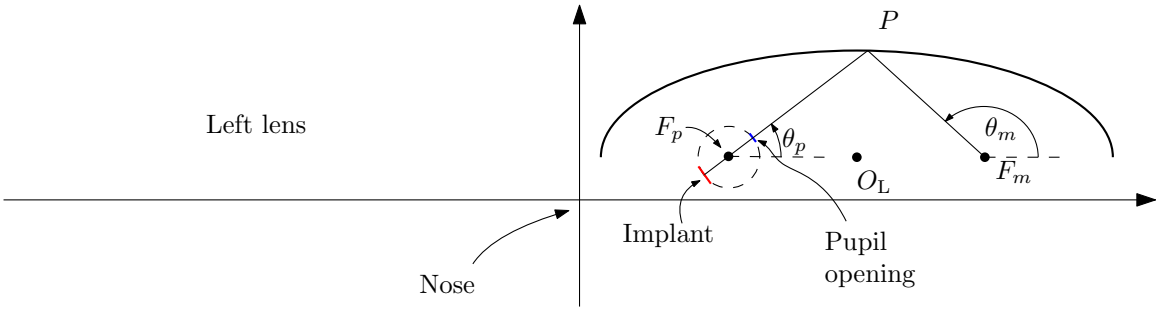

Figure 4.4: Two dimensional schematics of glasses with elliptical lenses.

with primes.

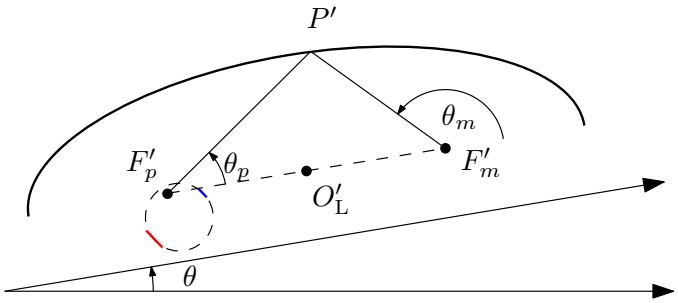

Figure 4.5: Schematics of the rotated lens.

Geometrically, the rotation can be described by the orthogonal matrix

$$\mathbf{R}(\theta) = \begin{pmatrix} \cos\theta & -\sin\theta \\ \sin\theta & \cos\theta \end{pmatrix} \tag{4.8}$$

In the rotated system, the mirror still directs the laser towards the other focus of the elliptical lens, which poses a problem since the eye does not rotate with the glasses. The laser is instead targeting the shifted focus, which is no longer aligned with the center of the eye globe. An example of a uncorrected laser path after a misalignment, along with the ideal corrected laser path which accounts for misalignment is illustrated within Figure 4.6.

A method to redirect the laser for a rotated lens is presented in Section 4.3, along with an analytic expression for the tolerance of the rotated system within which the redirected laser can power the implant. Tolerances depend on the rotation θ, and on the geometry of the system in terms of eye radius, pupil opening diameter, and PV cell size.

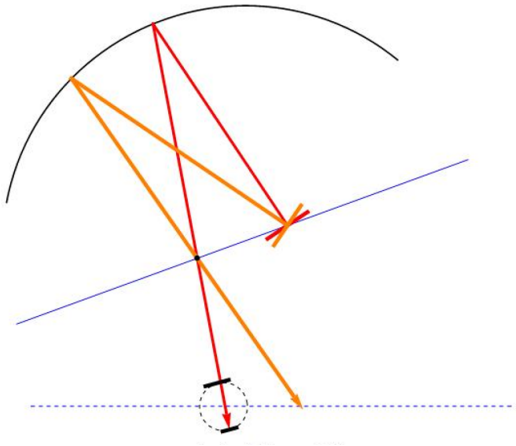

Figure 4.6: Example illustration of the effect of a 2D rotation disturbance on the laser beam path. The orange line displays the uncorrected laser path, and the red line displays an idea corrected laser beam path which accounts for the frame misalignment.

4.3 Misalignment compensation control for laser re-alignment

This section provides the development of a control algorithm to compensate for rigid body motions of the wearable devices and consequent misalignment of the laser, so that the laser beam is incident to the wireless implant when the glasses frame is within a tolerance that is dictated by the geometry of the system. The misalignment compensation control algorithm utilizes observations of the glasses frame orientation along with the geometric parameters of the glasses frame mounted system to determine the frame disturbance, and the adapted control action to take. Here, only the planar case is considered as disturbance.

The geometry of the system poses intrinsic constraints on the tolerance of misalignment compensation control to correct for the frame disturbance. The tolerance depends upon the distance between the default focus centered coincident with the ball center F_p and the focus' shifted position during disturbance F_p' as shown in Figure 4.7.

This shifted focus distance is quantified by the vector difference $\|\mathbf{r}_{F_p'} - \mathbf{r}_{F_p}\|$, which can be calculated from:

$$\mathbf{r}_{F_p'} - \mathbf{r}_{F_p} = (\mathbf{R}(\theta) - \mathbf{I})\,\mathbf{r}_{F_p} = (x_{O_L} - c)(\mathbf{R}(\theta) - \mathbf{I})\mathbf{e}_1 + y_{O_L}(\mathbf{R}(\theta) - \mathbf{I})\mathbf{e}_2 \tag{4.9}$$

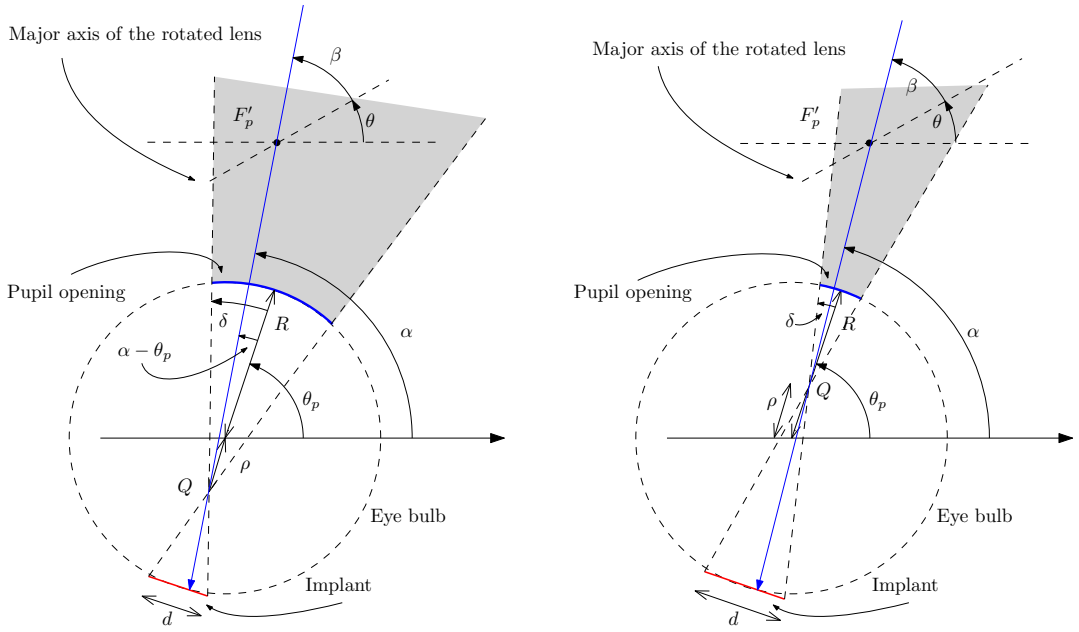

Figure 4.7: Schematic zoom of the eye for $\|\mathbf{r}_{F'_p} - \mathbf{r}_{F_p}\| > R$ for (a) $d < p$ and (b) $d > p$.

The vector norm is then obtained as

$$\|\mathbf{r}_{F'_p} - \mathbf{r}_{F_p}\| = \sqrt{\left((\mathbf{r}_{F'_p} - \mathbf{r}_{F_p}) \cdot \mathbf{e}_1\right)^2 + \left((\mathbf{r}_{F'_p} - \mathbf{r}_{F_p}) \cdot \mathbf{e}_2\right)^2} \tag{4.10}$$

From (4.9)

$$\begin{aligned}(\mathbf{r}_{F'_p} - \mathbf{r}_{F_p}) \cdot \mathbf{e}_1 &= (x_{O_L} - c)(\mathbf{R}(\theta) - \mathbf{I})_{11} + y_{O_L}(\mathbf{R}(\theta) - \mathbf{I})_{21} \\ &= (x_{O_L} - c)(\cos\theta - 1) + y_{O_L}\sin\theta \qquad (4.11)\\ (\mathbf{r}_{F'_p} - \mathbf{r}_{F_p}) \cdot \mathbf{e}_2 &= (x_{O_L} - c)(\mathbf{R}(\theta) - \mathbf{I})_{12} + y_{O_L}(\mathbf{R}(\theta) - \mathbf{I})_{22} \\ &= -(x_{O_L} - c)\sin\theta + y_{O_L}(\cos\theta - 1) \qquad (4.12)\end{aligned}$$

Substituting into (4.10)

$$\|\mathbf{r}_{F'_p} - \mathbf{r}_{F_p}\| = \sqrt{2\left((x_{O_L} - c)^2 + y_{O_L}^2\right)(1 - \cos\theta)} \tag{4.13}$$

4.3.1 Correction for shifted focus distance larger than the eye radius

With reference to Figure 4.7, let R be the radius of the eye ball. Graphically, the tolerance (i.e. the space where the laser beam can successfully target the implant) is represented by the shaded region. It is clear that if the focus F_p is mapped into the focus F'_p under an affine transformation, the MEMS mirror can direct the laser beam to the PV cell as long as the point F'_p falls within the shaded area. In order to obtain a quantitative test to establish if the displaced mirrored lens geometrically allows for the re-targeting of the laser beam to the implant, two conditions are identified, defined by $p < d$ (pupil opening smaller than chip size) and $p > d$ (pupil opening larger than implant size).

In order to quantify the tolerance, refer again to Figure 4.7. By approximating the pupil opening with the cord, the angle δ can be obtained by triangles similarity:

$$\tan\delta = \begin{cases} \dfrac{d/2}{R-\rho} = \dfrac{p/2}{R+\rho} & d < p \\ \dfrac{d/2}{R+\rho} = \dfrac{p/2}{R-\rho} & d > p \end{cases} \tag{4.14}$$

from which

$$\rho = \frac{R|d-p|}{p+d} \tag{4.15a}$$

$$\tan\delta = \frac{p+d}{4R} \tag{4.15b}$$

where p and d are respectively the pupil and the PV cell diameters. Therefore, in order to establish if the MEMS mirror tilt angle can be corrected to retarget the laser through the pupil opening to power the wireless implant, the following constraint must be satisfied

$$\theta_p - \delta < \alpha < \theta_p + \delta \tag{4.16}$$

or

$$|\alpha - \theta_p| < \delta \tag{4.17}$$

By observing that α is the angle between the vector $\mathbf{r}_{F'_p} - \mathbf{r}_Q$ and the horizontal axis,

we first obtain:

$$\mathbf{r}_Q = \mathbf{r}_{F_p} + \text{sgn}(d-p)\rho\left(\cos\theta_p \mathbf{e}_1 + \sin\theta_p \mathbf{e}_2\right) \tag{4.18}$$

$$\mathbf{r}_{F_p'} = \mathbf{R}(\theta)\mathbf{r}_{F_p} \tag{4.19}$$

Combining

$$\begin{aligned}\mathbf{r}_{F_p'} - \mathbf{r}_Q &= \left(\mathbf{R}(\theta) - \mathbf{I}\right)\mathbf{r}_{F_p} - \text{sgn}(d-p)\rho\left(\cos\theta_p \mathbf{e}_1 + \sin\theta_p \mathbf{e}_2\right) \\ &= \left(\mathbf{R}(\theta) - \mathbf{I}\right)\left((x_{O_\text{L}} - c)\mathbf{e}_1 + y_{O_\text{L}}\mathbf{e}_2\right) - \text{sgn}(d-p)\rho\left(\cos\theta_p \mathbf{e}_1 + \sin\theta_p \mathbf{e}_2\right)\end{aligned} \tag{4.20}$$

Therefore the slope $\tan\alpha$ with respect to the horizontal axis is given by

$$\tan\alpha = \frac{\left(\mathbf{r}_{F_p'} - \mathbf{r}_Q\right)\cdot \mathbf{e}_2}{\left(\mathbf{r}_{F_p'} - \mathbf{r}_Q\right)\cdot \mathbf{e}_1} \tag{4.21}$$

The expression in the numerator can be explicitly calculated as

$$\begin{aligned}&\left(\mathbf{r}_{F_p'} - \mathbf{r}_Q\right)\cdot \mathbf{e}_2 \\ &= (x_{O_\text{L}} - c)\mathbf{e}_2 \cdot \left(\mathbf{R}(\theta) - \mathbf{I}\right)\mathbf{e}_1 + y_{O_\text{L}}\mathbf{e}_2 \cdot \left(\mathbf{R}(\theta) - \mathbf{I}\right)\mathbf{e}_2 - \text{sgn}(d-p)\rho\sin\theta_p \mathbf{e}_2\cdot\mathbf{e}_2 \\ &= (x_{O_\text{L}} - c)\sin\theta + y_{O_\text{L}}(\cos\theta - 1) - \text{sgn}(d-p)\rho\sin\theta_p\end{aligned} \tag{4.22}$$

Similarly for the denominator

$$\begin{aligned}&\left(\mathbf{r}_{F_p'} - \mathbf{r}_Q\right)\cdot \mathbf{e}_1 \\ &= (x_{O_\text{L}} - c)\mathbf{e}_1 \cdot \left(\mathbf{R}(\theta) - \mathbf{I}\right)\mathbf{e}_1 + y_{O_\text{L}}\mathbf{e}_1 \cdot \left(\mathbf{R}(\theta) - \mathbf{I}\right)\mathbf{e}_2 - \text{sgn}(d-p)\rho\cos\theta_p \mathbf{e}_1\cdot\mathbf{e}_1 \\ &= (x_{O_\text{L}} - c)(\cos\theta - 1) - y_{O_\text{L}}\sin\theta - \text{sgn}(d-p)\rho\cos\theta_p\end{aligned} \tag{4.23}$$

Therefore the angle α can be calculated using the following expression, which includes the geometry of the system and the geometric disturbance in terms of the rigid body displacement of the reflective lens frame:

$$\tan\alpha = \frac{(x_{O_\text{L}} - c)\sin\theta + y_{O_\text{L}}(\cos\theta - 1) - \text{sgn}(d-p)\rho\sin\theta_p}{(x_{O_\text{L}} - c)(\cos\theta - 1) - y_{O_\text{L}}\sin\theta - \text{sgn}(d-p)\rho\cos\theta_p} \tag{4.24}$$

(Note that for $\theta = 0$, $\alpha = \theta_p$).

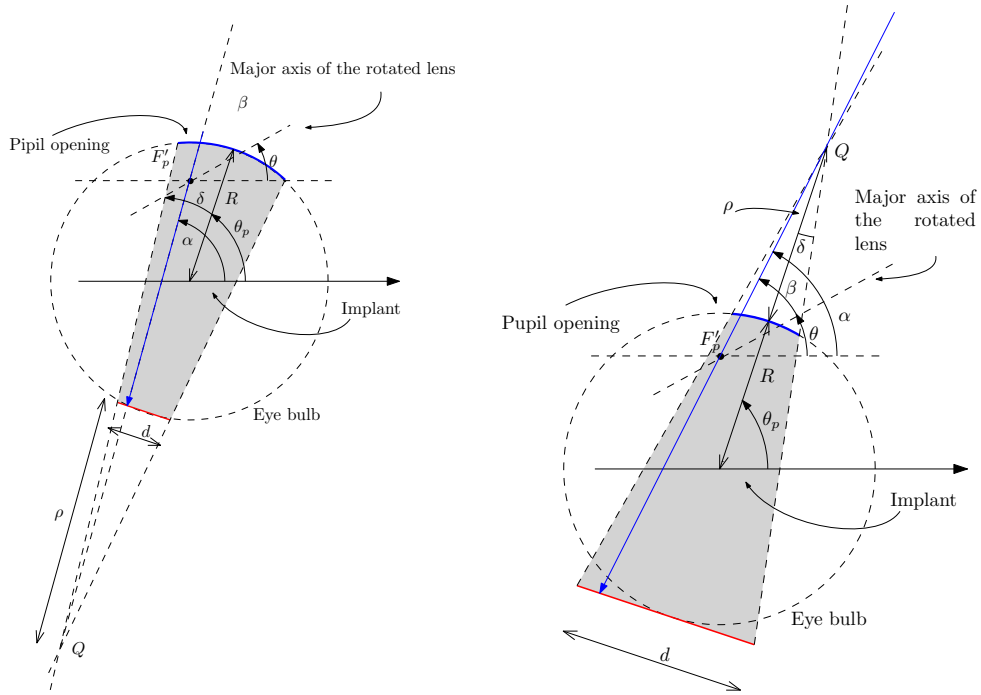

(a) (b)

Figure 4.8: Schematic zoom of the eye for $\|\mathbf{r}_{F'_p} - \mathbf{r}_{F_p}\| > R$ and (a) $p > d$; (b) $p < d$.

By referring again to Figure 4.7, given a rotational disturbance θ, the corrected MEMS mirror coordinate θ_m that accounts for the frame misalignment is calculated with expression (4.4) by replacing θ_p with the new coordinate β, calculated by:

$$\beta = \alpha - \theta \tag{4.25}$$

4.3.2 Correction for shifted focus distance norm smaller than the eye radius

With reference to Figure 4.8, the tolerance is graphically represented by the shaded areas.

With reference to Figure 4.8, by similarity of triangles the angle δ is obtained by

$$\tan\delta = \begin{cases} \dfrac{d/2}{\rho} = \dfrac{p/2}{\rho + 2R} & d < p \\ \dfrac{p/2}{\rho} = \dfrac{d/2}{\rho + 2R} & d > p \end{cases} \tag{4.26}$$

Solving for ρ, the angle can be expressed in terms of the system's geometric pa-

rameters as

$$\rho = \frac{2R\min(d,p)}{|d-p|} \tag{4.27}$$

$$\tan\delta = \frac{|d-p|}{4R} \tag{4.28}$$

The geometric condition for the MEMS mirror to be able to direct the laser to power the implant is

$$|\alpha - \theta_p| \leq \delta \tag{4.29}$$

By observing that α is the angle between the vector $\mathbf{r}_{F_p'} - \mathbf{r}_Q$ and the horizontal axis, the following expressions for these vector are first obtained

$$\mathbf{r}_Q = \mathbf{r}_{F_p} - (\rho + R)\,\mathrm{sgn}(d-p)\left(\cos\theta_p \mathbf{e}_1 + \sin\theta_p \mathbf{e}_2\right) \tag{4.30}$$

$$\mathbf{r}_{F_p'} = \mathbf{R}(\theta)\mathbf{r}_{F_p} \tag{4.31}$$

By following the same procedure as in Section 4.3.1 the following expression is derived

$$\tan\alpha = \frac{y_{O_L}(\cos\theta - 1) + (x_{O_L} - c)\sin\theta + \mathrm{sgn}(d-p)(\rho+R)\sin\theta_p}{(x_{O_L} - c)(\cos\theta - 1) - y_{O_L}\sin\theta + \mathrm{sgn}(d-p)(\rho+R)\cos\theta_p} \tag{4.32}$$

(Note that for $\theta = 0$, $\alpha = \theta_p$).

Given the rotational disturbance θ, the mirror coordinate θ_m can be calculated with expression (4.4) by replacing θ_p with the new MEMS coordinate β:

$$\beta = \alpha - \theta \tag{4.33}$$

4.3.3 Summary of the control algorithm for laser re-targeting

The control algorithm to compensate for the lens frame misalignment by re-targeting the laser through correction of the MEMS mirror tilt angles can be summarized as follows:

1. Given the geometrical parameters as shown in Figure 4.5, c, x_{O_L}, y_{O_L}, R, the geometric disturbance θ and the measured pupil coordinate θ_p calculate the shifted focus distance $\|\mathbf{r}_{F_p'} - \mathbf{r}_{F_p}\| = \sqrt{2\left((x_{O_L} - c)^2 + y_{O_L}^2\right)(1 - \cos\theta)}$.

2. If $\|\mathbf{r}_{F_p'} - \mathbf{r}_{F_p}\| > R$

   (a) Calculate

   $$\rho = \frac{R|d-p|}{p+d}$$
   $$\tan\delta = \frac{p+d}{4R}$$

   (b) Calculate α:

   $$\tan\alpha = \frac{(x_{O_L}-c)\sin\theta + y_{O_L}(\cos\theta - 1) - \mathrm{sgn}(d-p)\rho\sin\theta_p}{(x_{O_L}-c)(\cos\theta-1) - y_{O_L}\sin\theta - \mathrm{sgn}(d-p)\rho\cos\theta_p}$$

   (c) The laser can be redirected to the implant provided that

   $$|\alpha - \theta_p| \leq \delta$$

   (d) Calculate the corrected MEMS mirror coordinate θ_m by replacing θ_p with the angle $\beta = \alpha - \theta$ in (4.4):

   $$\sin(\theta_m - \beta) - e(\sin\theta_m + \sin\beta) = 0$$

3. If $\|\mathbf{r}_{F_p'} - \mathbf{r}_{F_p}\| \leq R$:

   (a) Calculate

   $$\rho = \frac{2R\min(d,p)}{|d-p|}$$
   $$\tan\delta = \frac{|d-p|}{4R}$$

   (b) Calculate α:

   $$\tan\alpha = \frac{y_{O_L}(\cos\theta-1) + (x_{O_L}-c)\sin\theta + \mathrm{sgn}(d-p)(\rho+R)\sin\theta_p}{(x_{O_L}-c)(\cos\theta-1) - y_{O_L}\sin\theta + \mathrm{sgn}(d-p)(\rho+R)\cos\theta_p}$$

   (c) The laser can be redirected to the implant provided that

   $$|\alpha - \theta_p| \leq \delta$$

   (d) Calculate the corrected MEMS mirror coordinate θ_m by replacing θ_p with

the angle $\beta = \alpha - \theta$ in (4.4):

$$\sin(\theta_m - \beta) - e(\sin\theta_m + \sin\beta) = 0$$

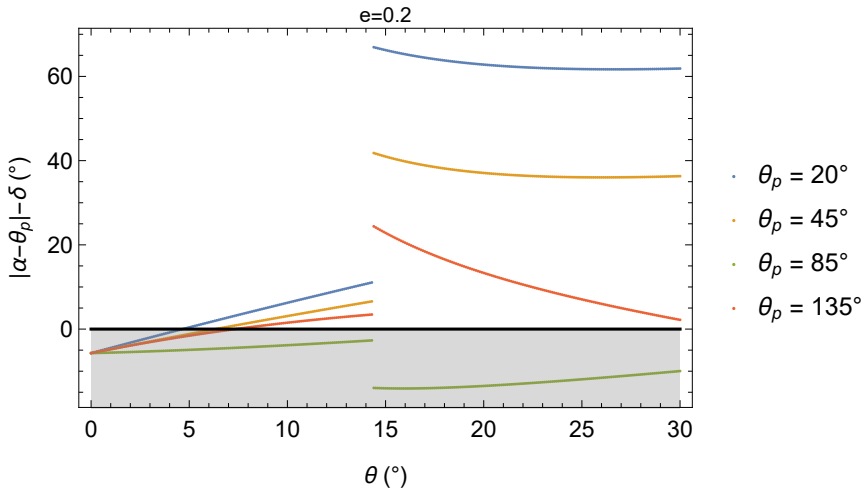

Figure 4.9: Curves $|\alpha - \theta_p| - \delta$ versus θ for eccentricity $e = 0.2$. The shaded area indicates geometric configuration that allow to power the implant.

For ellipses lens' eccentricity $e = 0.2$, curves of the function $|\alpha - \theta_p| - \delta$ versus the disturbance θ are shown in Figure 4.9. If this quantity (the tolerance function output) is negative (grey shaded area), the geometric and physical configuration of the system allow the MEMS mirror to re-target the laser beam to the implant; on the other hand, if this quantity is positive it is not possible to re-target the laser to the implant. As expected, a forward looking gaze nearly "straight-ahead" ($\theta_p = 85°$) is very tolerant to disturbances, whereas peripheral gaze angles are less tolerant as clearly shown by the related curves crossing more into the region corresponding to positive tolerance function output values. The discontinuity in the curves is due to the discontinuity in the shaded area in Figures 4.7 and 4.8, transitioning from the two geometric cases corresponding respectively to the lens focus initially occupied by the pupil to be mapped inside or outside of the eye ball region. In the following Section, a continuous case that arises from the more restricted condition of re-targeting the laser to the center of the implant only, rather than anywhere on the implant area.

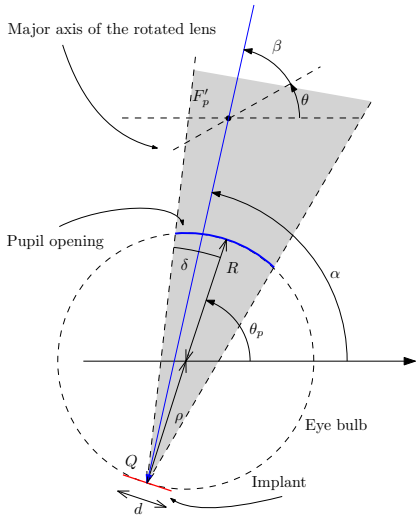

Figure 4.10: Schematic zoom of the eye with laser redirected to the center, described by the geometric condition $d = 0$.

4.3.4 Re-targeting the laser to the center of the implant

The misalignment compensation control algorithm may be modified to the more restricted case where the laser beam must target only the center of the implant, as opposed to the more relaxed geometric conditions where the laser beam may target anywhere on the implant. The geometry corresponding to this case, shown in Figure 4.10, can be seen as a special case of the geometry in Figure 4.12. With $d = 0$, the two cases discussed in Section 4.3.1 and Section 4.3.2 reduce to the same geometry in terms of feasible laser directing region, regardless of the relative size $d - p$. Therefore, the curves of the tolerance function $|\alpha - \theta_p| - \delta$ versus the disturbance θ become continuous, as shown in Figure 4.11, unlike those shown in Figure 4.9. Equations (4.15) become

$$\rho = R \tag{4.34a}$$

$$\tan\delta = \frac{p}{4R} \tag{4.34b}$$

The angle α is given by

$$\tan\alpha = \frac{(x_{O_L} - c)\sin\theta + y_{O_L}(\cos\theta - 1) + R\sin\theta_p}{(x_{O_L} - c)(\cos\theta - 1) - y_{O_L}\sin\theta + R\cos\theta_p} \tag{4.35}$$

and the new MEMS mirror tilt angle is calculated as

$$\beta = \alpha - \theta \tag{4.36}$$

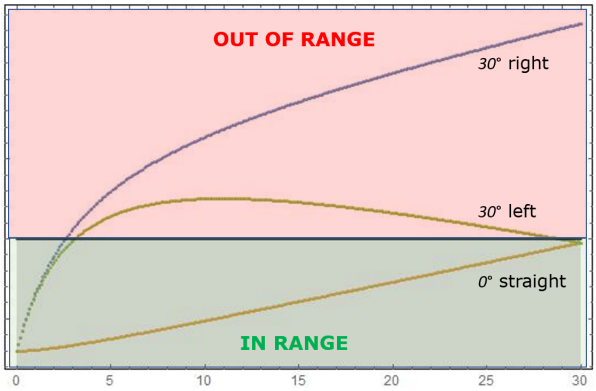

Figure 4.11: Curves $|\alpha - \theta_p| - \delta$ versus θ for eccentricity $e = 0.2$, when the control action is restricted to target the center of the implant.

4.4 Discussion of simulation results

To illustrate the action of the laser re-targeting algorithm, simulation results are produced by considering the case of rigid body motion of the glasses frame. Within the presented simulation results, the power delivered to the implant is quantified and compared between two cases, respectively characterized by the presence and action of the control algorithm compared to its absence. The simulation environment is similar to the one introduced in Section 3.4, with the addition of a model for the geometry of the ellipsoidal lens, the laser beam path, and the pupil opening. iBIONICS provided an ellipse eccentricity of $e = 0.359$, and major axis length of 45 mm for the cross section of the ellipsoidal reflector lens. The change of the the beam width at the intersection point of the PV cell due to the geometric disturbance of the glass frame is also modelled by a simple set of optical equations, as described in Appendix A. The variations of the beam width size (less than ± 0.2 mm) have negligible impact on the amount of power delivered to the implant. The parameters for the representative simulation are found in Table 4.1. Three iterations of the simulation are presented, with the rotational disturbance being varied between $5^\circ, 10^\circ, 15^\circ$, corresponding to Figures 4.12, 4.13 and 4.14.

By comparing Figures 4.12, 4.13 and 4.14, it is obvious that if the geometric disturbance θ increases the ability of the MEMS mirror controller to target the wireless

Parameter	Symbol	Value
Process noise (acceleration magnitude)	a_k	$1000^\circ/s^2$
Measurement noise covariance matrix	$\mathbf{R}_k$	$\begin{bmatrix} 1^\circ & 0 \\ 0 & 1^\circ \end{bmatrix}$
Laser beam width	σ	$1.5mm +/- 0.2mm$
Simulation interval rate	$\frac{1}{\Delta t}$	240 Hz
Observation sampling rate	$\frac{1}{\Delta t_{meas}}$	120 Hz
PV cell square boundary length	L	2 mm
Laser beam maximum intensity	I_{max}	$2.55\frac{mW}{mm^2}$
PV cell conversion efficiency	η_{PV}	95%
Ellipse eccentricity	e	0.359
Ellipse major axis length	a	45 mm
Frame disturbance magnitude	θ	Varied: $5^\circ, 10^\circ, 15^\circ$
Distance from frame nose pad to eye ball	$L_{eyespace}$	40 mm
Pupil opening	d_p	3 mm

Table 4.1: Parameters for simulation with frame disturbance.

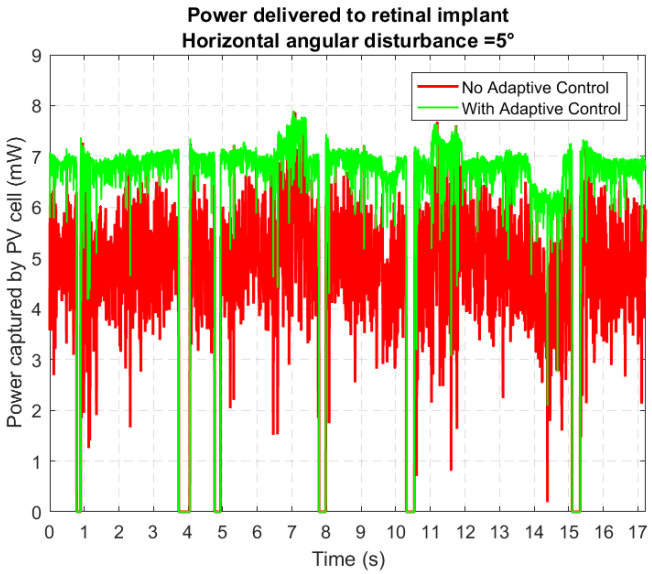

Figure 4.12: Results of implant tracking simulation where a glasses frame disturbance is present, with magnitude $\theta = 5^\circ$.

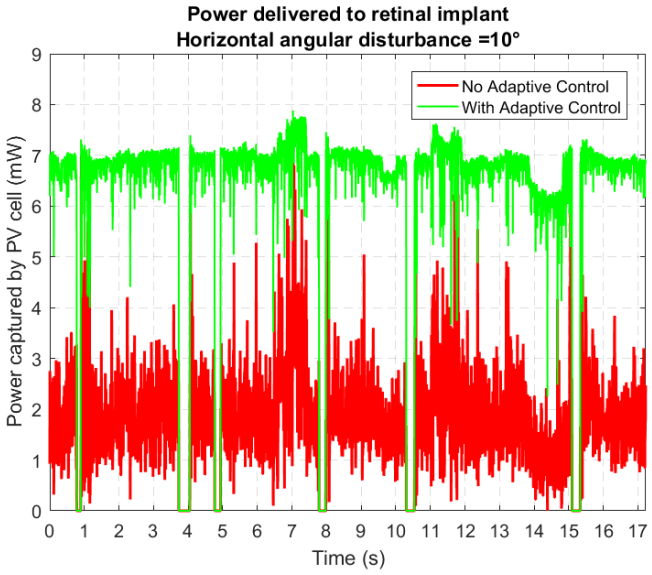

Figure 4.13: Results of implant tracking simulation where a glasses frame disturbance is present, with magnitude $\theta = 10°$.

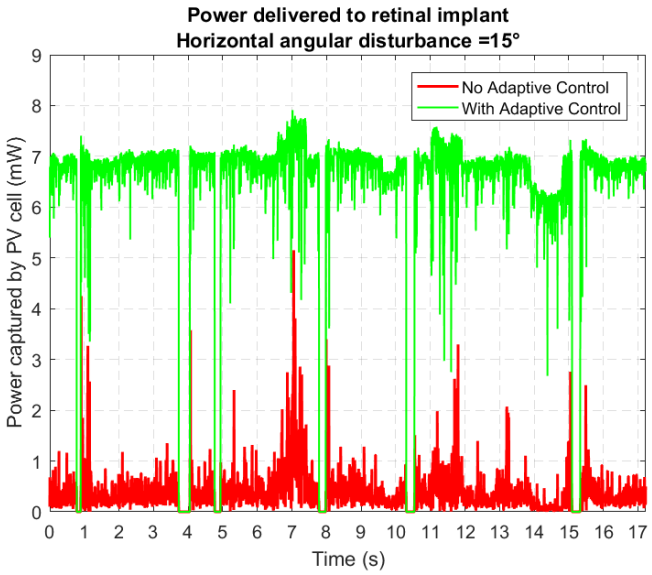

Figure 4.14: Results of implant tracking simulation where a glasses frame disturbance is present, with magnitude $\theta = 15°$.

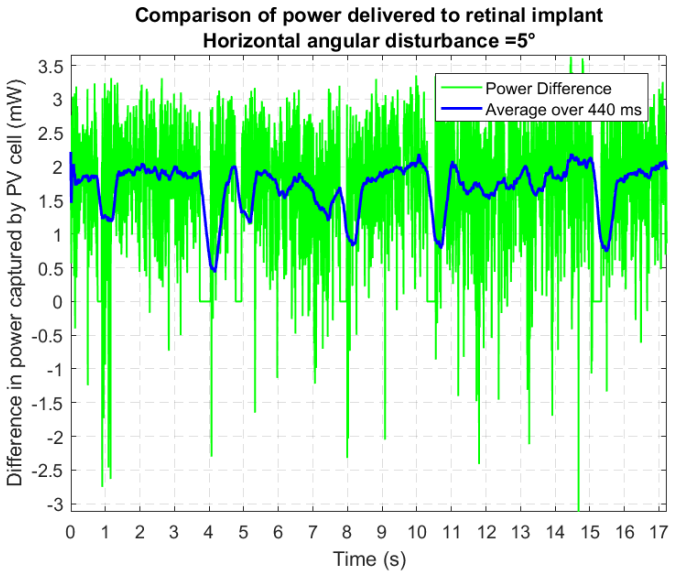

Figure 4.15: Comparison of power delivered to implant, with misalignment compensation control algorithm against without. A glasses frame disturbance is present with magnitude $\theta = 5°$.

implant is significantly reduced. With an angular disturbance exceeding 5°, the power system is unable to consistently power the wireless implant. For all three presented simulations, the inclusion of the misalignment compensation control algorithm corrects for the disturbance resulting in consistent power to the implant above the 5 mW threshold (with the exception of sudden fast eye saccades and blinks), outright negating the impact of the glasses frame disturbance. To quantify the effective improvement when using the misalignment compensation control algorithm in the event of the disturbance of the frame, the difference of the power delivered with misalignment compensation control against without misalignment compensation control is compared in Figures 4.15, 4.16 and 4.17.

The mean and standard deviation for each power curve over the simulation time (excluding blink events) is shown in Table 4.2. There is a clear trend shown that the increased disturbance angle results in significantly worse power delivery if no misalignment compensation control is used. When the misalignment compensation control algorithm is used, the mean power delivered is consistently above 6.75 +/- 0.60 mW. When not using the misalignment compensation control algorithm, the mean power loss varies from 27% at 5° disturbance up to 95.5% at maximum studied disturbance of 15°.

An important feature of the proposed misalignment compensation control algorithm lies in its added tolerance to the glasses frame disturbance. The misalign-

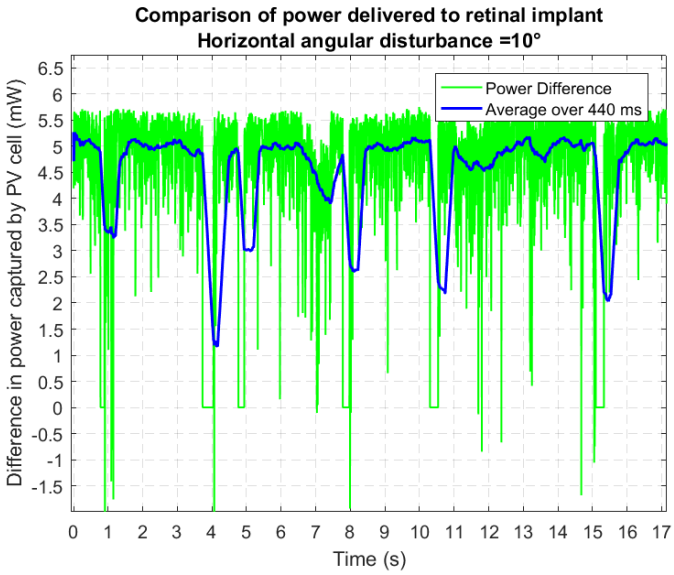

Figure 4.16: Comparison of power delivered to implant, with misalignment compensation control algorithm against without. A glasses frame disturbance is present with magnitude $\theta = 10°$.

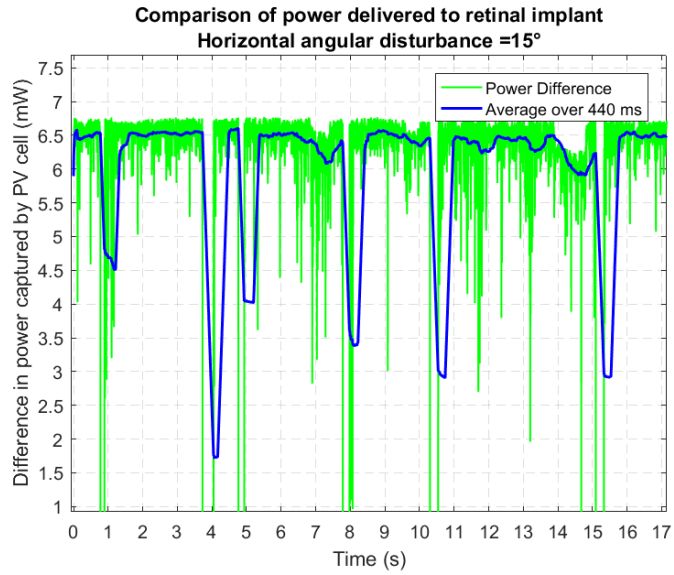

Figure 4.17: Comparison of power delivered to implant, with misalignment compensation control algorithm against without. A glasses frame disturbance is present with magnitude $\theta = 15°$.

Compensation?	Disturbance θ	Mean +/- Std dev	% Improvement
Yes	5°	6.80 +/- 0.60 mW	36.8%
No	5°	4.97 +/- 0.96 mW	–
Yes	10°	6.78 +/- 0.61 mW	260.6%
No	10°	1.88 +/- 0.82 mW	–
Yes	15°	6.76 +/- 0.61 mW	1727.0%
No	15°	0.37 +/- 0.33 mW	–

Table 4.2: Comparison of mean and standard deviation of power delivered to implant during simulation, with glasses frame disturbance.

ment compensation control algorithm calculates the region of the PV cell that is not occluded by the pupil opening when the glasses frame is disturbed off axis, and then directs the laser beam path to intersect the center of the non-occluded region. This feature ensures that if the eye begins to rotate, the laser beam will remain on the PV cell for more time than in the case where the the laser beam path is restricted to targeting only the true center of the PV cell, as described in Section 4.3.4. The simulations results shown in Figures 4.18, 4.19 and 4.20 show the amount of power delivered over time where the misalignment compensation control algorithm is restricted to targeting only the center of the PV cell. These simulation's environment are identical to those shown in Figures 4.12, 4.13 and 4.14, with the key difference being the center of PV cell restriction. This comparison solidifies that the performance of the implant tracking in the event of the glasses frame being misaligned is significantly worse without algorithmic compensation that accounts for it.

For all three examined simulation cases where the center of the PV cell is the target the standard deviation is 17-40% of the mean, indicating power delivery is not consistent. This result further supports the advantage of the proposed misalignment compensation control algorithm, in that the provided tolerance feature ensures optimal implant tracking. The results for the test are summarized in Table 4.3.

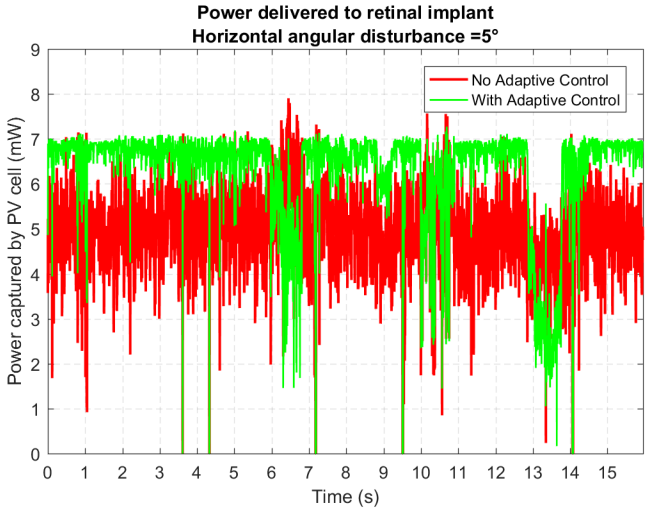

Figure 4.18: Results of implant tracking simulation when the misalignment compensation control algorithm is only able to target the center of the implant, and a glasses frame disturbance is present, with magnitude $\theta = 5°$.

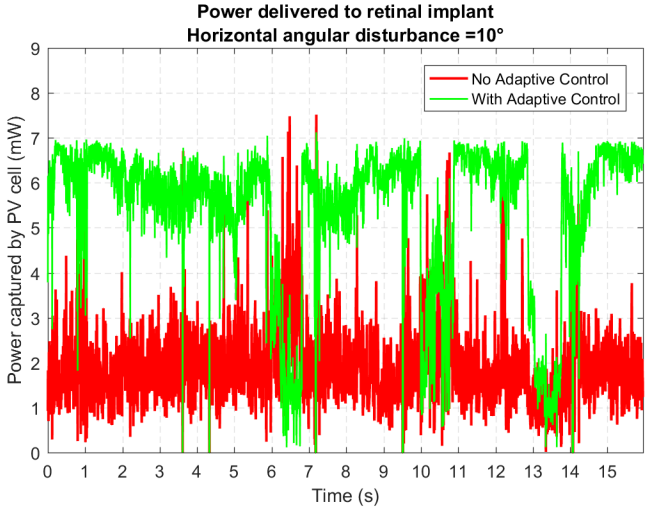

Figure 4.19: Results of implant tracking simulation when the misalignment compensation control algorithm is only able to target the center of the implant, and a glasses frame disturbance is present, with magnitude $\theta = 10°$.

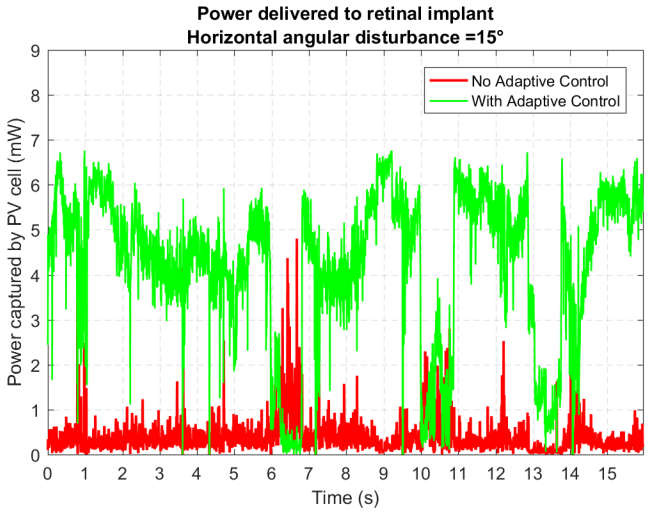

Figure 4.20: Results of implant tracking simulation when the misalignment compensation control algorithm is only able to target the center of the implant, and a glasses frame disturbance is present, with magnitude $\theta = 15°$.

Compensation?	Disturbance θ	Mean +/- Std dev	% Improvement
Yes	5°	6.29 +/- 1.12 mW	28.4%
No	5°	4.9 +/- 0.97 mW	–
Yes	10°	5.39 +/- 1.62 mW	180.7%
No	10°	1.92 +/- 0.82 mW	–
Yes	15°	4.22 +/- 1.69 mW	1010.5%
No	15°	0.38 +/- 0.36 mW	–

Table 4.3: Comparison of mean and standard deviation of power delivered to implant during simulation, with glasses frame disturbance. misalignment compensation control algorithm is restricted to targeting the center of the PV cell only.

Chapter 5

Conclusions and Future Work

5.1 Conclusions

In this work, a laser targeting system was developed to provide power and visual scene data to a wireless retinal implant. In Chapter 2, a literature review provides context for the most common retinal pathologies causing vision loss in Canadians, and the retinal implants that are being developed to provide those affected with visual prosthesis. In addition, an introduction to the characteristics of human eye motion for the purpose of eye tracking was provided. In Chapter 3, a predictive eye implant tracking system was developed which uses a Kalman filter and a pupil tracking camera to produce state estimates of the position of the eye, in order to direct a laser beam by steering a micro-electro-mechanical system (MEMS) mirror to the photovoltaic (PV) cell on the implant mounted to the back of the eye. A series of MATLAB simulations were used to assess the viability of the design to power the wireless retinal implant during regular eye motion. The amount of power delivered to the retinal implant received by the laser beam falling on the PV cell was calculated as means to comment on the effectiveness of the implant tracking solution. In collaboration with the University of Ottawa SUNLAB, the control system and the predictive tracking algorithm were tested on an experimental platform. In Chapter 4, a misalignment compensation control algorithm was presented to compensate for the glasses frame and laser beam becoming misaligned from the eye. A model for the geometric and optical system consisting of an ellipsoidal reflector lens, the pupil lens, and the MEMS mirror was provided, along with a set of design tools that describe the tolerance of the misalignment compensation control algorithm to varying magnitudes of glasses frame misalignment. A set of

simulations were produced to demonstrate the effectiveness of the misalignment compensation control algorithm to improve the power delivered to the implant during misalignment events.

The ability of the system to track the implant as the patients eye moved about was quantified through simulation, as well as by an experimental prototype system, as described in Chapter 3. It was found that a MEMS mirror may be controlled quickly enough to track the implant beyond the pupil opening when combined with a low cost common eye tracking camera. It was demonstrated that by augmenting the MEMS mirror controller with a Kalman filter based predictive tracking algorithm, the implant tracking performance and resulting power delivery to the implant is improved to the point that the laser system is able to consistently power the retinal implant. The predictive tracking algorithm filters the measurement error caused by the eye tracking camera, and provides improved state estimates of the true position of the implant during eye motion. Simulations with real eye motion were performed. It was found that the camera eye position measurement system must have a framerate of at minimum 30 fps to ensure that power to the implant is consistently above the 5 mW threshold for stimulation. To match the experimental system, by simulating for a measurement error of 2 mm, and a camera framerate of 60 fps, the simulation suggests that with the predictive tracking algorithm would provide mean power delivered to the implant of 7.13 +/- 0.70 mW. The predictive tracking algorithm provides power improvement of on average 13.8% over the measurement only approach for the measurement error of 8 mm, the highest measurement error considered. The experimental system provided results that demonstrated a 50% reduction to the spatial misalignment of the laser beam to the PV cell center by using the predictive tracking algorithm.

The implant tracking solution was further augmented by a misalignment compensation control algorithm to compensate for geometric disturbances caused by the glasses frame moving relative to the eye during everyday use cases, described in Chapter 4. As part of the algorithm, analytic expressions for system's tolerance to disturbance were developed. These expressions quantify in terms of the geometric parameters and rigid body motion parameters (disturbances) the limits beyond which it is not possible to re-target the laser to the implant, therefore also providing design tools. When a glasses frame disturbance occurs, the MEMS mirror can fail in its attempt to position the laser beam to intersect the pupil opening to target the implant if no corrective action is taken. With a horizontal frame disturbance of just 5°, the mean power delivery to the implant falls below the 5 mW

allowable threshold. By applying the misalignment compensation control algorithm to the MEMS mirror controller, the corrected mirror target coordinates result in a consistent power delivery of above 6.75 +/- 0.60 mW for frame disturbance angles as high as 15°. The power improvement with the application of the misalignment compensation control algorithm ranged from 36% for a 5° disturbance, up to 1827% for 15° disturbance, the maximum studied.

5.2 Future work

In the future, the design of the implant tracker by control of the MEMS mirror to redirect the laser beam may be further improved in several ways.

A current limitation of the predictive tracking algorithm lies in the state transition model for eye motion, in particular how the acceleration of the eye is modelled. Eye acceleration was a minor consideration within the work, as the timescale that eye acceleration occurs over is lower than the minimum timescale considered for the implant tracking algorithms. The current state transition model treats the pupil as a kinematic point mass that moves with constant velocity between two updating times (or within each discrete time interval, where a zero velocity corresponds to eye fixation. The acceleration of the eye as it shifts between the identified eye motion modes (fast saccades, smooth pursuit, and fixation) is modelled as the process noise, with magnitude of $10^{3^\circ}/s$ to match that of real eye motion. In the future, a full model of eye motion which includes the probability of a eye velocity change and the corresponding eye acceleration rate may be implemented. For example, in the work [55], where an improved full eye motion model is presented that incorporates the amplitude of saccades, acceleration cues and the visual stimulus to improve predictions of the movement of the eye.

The standard Kalman filter algorithm is restricted to the estimation of linear systems. While eye motion is may be primarily identified as a linear system, proper treatment of eye acceleration and saccade amplitudes requires a non-linear dynamic model. To address this, the Kalman filter algorithm may be modified to account for the random eye accelerations by modelling changes the motion of the eye as a mean reverting stochastic differential equation with discontinuous jumps. The probability of an acceleration occurring as time progresses is captured in the model by a random variable, which returns to the mean value after a jump in velocity occurs. An example of a similar state transition model is described within [56] to model the random motion of the zebrafish. The prediction of the nonlin-

ear eye motion may also be accomplished through an extended Kalman filter, or through non-linear auto-regressive models generated by reinforcement learning algorithms. In particular, the use of reinforcement learning algorithms to determine areas of interest within the visual scene would provide a means to predict how the eye may survey the scene, and predict the eye motion path accordingly [57].

Appendix A

Gaussian Laser Beam

As part of a prior collaborative study with iBionics, R. Cheriton of the University of Ottawa SUNLAB validated that a laser beam with a Gaussian distribution would offer consistent power delivery while allowing some tolerance to misalignment of the laser beam. The laser beam width was defined by the full width at half maximum convention, where at the bounds of a circular area, laser irradiation intensity is half of the maximum irradiation intensity at the center of the Gaussian curve. The intensity of the laser beam at a distance r from the center of the laser beam is defined by the laser irradiation intensity function

$$P_r = I_{max} \exp \frac{r^2}{2\sigma^2} \tag{A.1}$$

where I_{max} is the maximum laser intensity at the center of the Gaussian beam, r is the radius from the laser beam center to a point on a 2D flat surface, and σ is the laser beam width, defined by the radial distance from the center of the laser beam where the irradiation drops to half of the maximum power at the center. A sample render showing the distribution of a Gaussian laser beam irradiation over a 2D area is shown in Figure A.1.

The laser beam width on the implant may vary when the eye or the glasses frame move. The laser beam width on the implant was determined by the following sequence of optical image distance and lens magnification calculations. First, the optical distance to the image of the laser reflected by the ellipsoidal reflector is determined by

$$d_{ell} = ({f_e}^{-1} - {d_m}^{-1})^{-1} \tag{A.2}$$

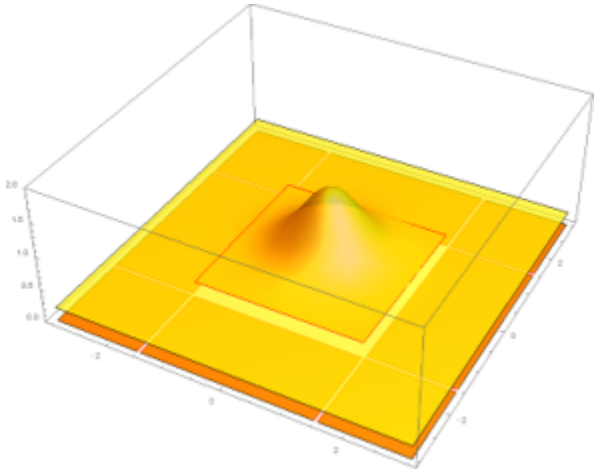

Figure A.1: 3D render of Gaussian laser beam with a beam width of 1 mm, where the height of the function corresponds to the irradiation intensity of the laser beam over a 2D spatial area. (Courtesy R. Cheriton)

where d_{ell} is the optical distance of the laser image reflected by the ellipsoidal reflector, f_e is the ellipsoidal lens focal length, and d_m is the optical distance of the image of the laser on the MEMS mirror, from infinity (where the laser emitter resides).

Next, the optical distance to the image of the laser on the pupil lens is determined by

$$d_p = ({f_p}^{-1} - (d_{ell} - (r_p - r_{eye}))^{-1})^{-1} \tag{A.3}$$

where d_p is the optical distance of the laser image reflected by the pupil lens, f_p is the pupil lens focal length, r_p is the spatial distance from the laser reflection point on the ellipsoidal lens to the pupil lens, and r_{eye} is the eye diameter. The eye diameter is equal to the distance from the the pupil opening to the implant on the retina.

By the lens magnification equation the resulting beam width of the laser on the implant is determined by

$$\sigma_i = \frac{d_p}{(d_{ell} - (r_p - r_{eye}))) \times \sigma_o} \tag{A.4}$$

where σ_i is the beam width on the implant, and σ_o is the original beam width of the laser at the emission point.

Within the MATLAB simulations and the experimental set up, f_p was set to

17 mm and f_e was set to 18 mm. Within Chapter 3, σ_i was selected to be 1.5 mm. Within Chapter 4, σ_o was selected to be 1.5 mm, resulting in a σ_i with mean 1.17 mm and a standard deviation of 0.11 mm. The range of laser beam width sizes on the implant varied between a minimum of 00.88 mm and a maximum of 1.75 mm.

Appendix B

Code for MATLAB Simulation

The code below is a script written in MATLAB, to simulate the implant and the laser and they move with respect to a patient's eye motion. The eye motion is captured from real eye motion samples, with a method described in Appendix C. The simulation compares tracking performance of the different algorithm and simulation environments by calculating the power delivered to the implant. A description of the optical system and Gaussian laser beam is found in Appendix A.

Listing B.1: Matlab code to simulate implant tracking

```
1  %% This program combines the work from BEAMTASK for pupil tracking
       and power simulation with a Kalman Filter, and the work
2  % from BLINKER involving adaptive control in the event of a
       horizontal
3  % rotation of the glasses frame.
4
5  %% The program works in the following way:
6  % 1) For each time step K, a true pupil position is read from a time
       history file
7  % 2) The Kalman Filter iterates and an estimate is made. A
       measurement may occur.
8  % 3) A rotational disturbance is applied, which pertubes the position
        of the laser target relative to the eye...
9  %  this is represented by adding the disturbance contribution to the
       horizontal position
10 % 4) The new targeted position with disturbance applied is used for
       the power calculation.
11
12 %% Pupil tracking and Laser power capture simulation
```

```
13
14 function main()
15 close all;
16 clc;
17
18 %% QUICK TOGGLE OPTIONS
19 % Plots to display
20 animationmotion = 0;
21 powerplot = 1;
22 Pnormplot = 0;
23
24 % Options
25 KFoper = 1; %KF On or off
26 adaptcontrol = 0;
27 plotlens = 0;  %Plot lens, mirror, eye and implant diagram
28
29 % Degrees of disturbance
30 thetadis = 0;
31 thetadis_orig = thetadis;
32
33 %% True Motion
34 X_true = (import_motion_data())';
35
36 % del_t gives the time between measurements of the pupil state.
37 Hz = 240;       %Time between pupil state updates
38 del_t = 1/Hz;
39 %% GUASSIAN BEAM CALC
40 % ASIC spec (safe time 440 ms, use 300 ms)
41 safe_t = 0.440; %300 ms
42 range = floor(safe_t/del_t);
43 %Beam and PV Cell parameters
44 maxpower=2.55;  %in mW/mm^2 this is the peak power at the centre of
      the gaussian
45 domainsize=10;  %in mm  this is the width of the calculation region
      where calculation takes place
46 PVwidth=2; %in mm
47 PVlength=2; %in mm
48 pvefficiency=1;
49
50 horzeyediameter=24;  %horiztonal eye diameter
51 horzeyeradius=horzeyediameter/2; %horiztonal eye radius
52 verteyediameter=24; %vert eye diameter
53 verteyeradius=verteyediameter/2; %vert eye radius
```

```
54
55 precision=10;  %keep it at 10 for quick and dirty calculations
56 %1/precision  is the unit cell size in mm. so 10 means 100um cell
       sizes
57 %make it 50-100 if you're getting a sandwich and coffee (20um to 10um
58 %resolution)
59 %make it 1000 if you want to take a nap (1 um resolution)
60
61 %Make conversions
62 pvcellwidth=PVwidth*precision;
63 pvcelllength=PVlength*precision;
64 size=domainsize*precision;
65
66 %% Intializaton for Kalman Filter
67 %Initialize estimated state vector, where: X = [x-pos,y-pos,x-vel,y-
       vel] of pupil.
68 X = [0;0;1;1];
69 %Set previous position to be initial position of tracker.
70 X_prev = [0;0;0;0];
71 X_prev2 = [0;0;0;0];
72
73 % F is a linear function, where X(k+1) = F(X(k)) + u[k]
74 F = [1 0 del_t 0;0 1 0 del_t;0 0 1 0; 0 0 0 1];
75 % u[k] is known system noise, given as V[k]*del_t, and V[k]=d_X/d_t[k
       ]
76
77 % The initial error covariance matrix is defined
78 P = [0.1984         0    3.9635         0;
79           0    0.1984         0    3.9635;
80      3.9635         0  173.8183         0;
81           0    3.9635         0  173.8183];
82
83 %Q is the process noise covariance matrix, as defined by given
       variance of
84 %pupil position change.
85 %For now, we use strictly x and y variance values on their own
86 Qx = 1000000;
87 Qy = 1000000;
88 Q = [Qx 0; 0 Qy];
89
90 % Define G
91 G = [del_t^2 0; 0 del_t^2; del_t 0; 0 del_t];
92 %Measured Error
```

```
93  %Sig Measure
94  R = [0.5 0;0 0.5];      %error +/- 0.707
95  %Kalman gain
96  K = [0 0;0 0;0 0;0 0];
97  y = [0;0];
98  %Measurement Matrix
99  H = [1 0 0 0; 0 1 0 0];
100 %Z prev
101 Z_prev = [0;0];
102 n = length(X_true(1,:));
103 % Movie properties
104 real_time = n*(del_t);
105
106 %% Begin iterations
107 Xt_buff = zeros(2,n);
108 X_blinks = zeros(1,n);
109 X_buff = zeros(2,n);
110 X_buff(:,1) = X_prev([1 2]);
111 Z_buff = zeros(2,n);
112 VE_buff = zeros(2,n);
113 E_buff = zeros(2,n);
114 norm_error = zeros(1,n);
115 meas_occur = 0;
116
117 %Define arrays
118 pvcellpower=zeros(size,size);
119 beam=zeros(size,size);
120 cell=zeros(size,size);
121 halfsize=size/2;
122 totalpower=zeros(1,n);
123 avg_power=zeros(1,n);
124 P_buff = zeros(1,n);
125 K_buff = zeros(1,n);
126
127 %Q Iteration loop. Stores values of Average power as Q changes
128 AP_buff = [];
129 Q_buff = [];
130 P_buff = [];
131
132 %%% The first loop is used purely to iterate over several Q values,
      and can
133 %%% be neglected
134 Xt_prev = [0;0];
```

```
135 blink = 0;
136 beamwidth_buff = [];
137 random_meas_error = zeros(2,n);
138 % for k=1:n
139 %    random_meas_error(:,k) = diag(normrnd(zeros(2),R));;
140 % end
141
142 % Run sim twice to store power calcs for with vs without
143 for m =1:2
144
145 if m == 1
146     KFreset = 0;
147 elseif m == 2
148     KFreset = 1;
149 end
150
151 %%% This is the main loop. It must run to produce results
152 for k=1:n
153
154     %% Predictor - Corrector Algorithm (KALMAN FILTER)
155     %To simulate space between measurements, we add a simple check
        for
156     %current time step. Multiples of x trigger measurements. Ex.
        every 4
157     %time steps there is a measurement.
158     %If true time step 1/Hz, measurements occur
159
160     %** This If statement decides if a measurement occured for
        simulation.
161     %For the experimental test bench, you would send a measurement
        command
162     %only if you have recieved one
163     interval = 3;
164     %% Checking and taking measurement
165     if (¬rem(k,interval))
166         meas_occur = 1;
167     else
168         meas_occur = 0;
169     end
170
171     X_true(:,k) = X_true(:,k)+diag(normrnd(zeros(2),R));
172
173     if (meas_occur)
```

```
174         if (any(isnan(X_true(:,k))))
175             X_blinks(k) = 1;
176             blink = 1;
177             Z = [0;0];
178             Z_buff(:,k) = Z_prev;
179             meas_occur = 0;
180         else
181             blink = 0;
182             Z = (X_true(:,k));
183             Z_prev = Z;
184             Z_buff(:,k) = Z;
185         end
186     else
187         Z = [0;0];
188         Z_buff(:,k) = Z_prev;
189     end
190     %% Pupil Tracker Operation
191     if (KFoper)
192      % PREDICT STEP
193     %Predict current state from pupil motion model
194     X_temp = F*X;
195     %Predict current P from previous data.
196     P_temp = F*P*F' + G*Q*G';
197     %** Z Is the measurement you have taken**
198
199     %UPDATE STEP
200     % Calculate Kalman Gain
201     if (meas_occur)
202         y = Z-H*X_temp;
203         S = R + H*P_temp*H';
204         K = (P_temp*H'*(inv(S)));
205
206         X = X_temp + K*(y);
207         P = (eye(4) - K*H)*P_temp;
208     else
209         X = X_temp;
210         P = P_temp;
211     end
212
213     % Take norm of P, store in buff
214     P_buff(k) = norm(P,'fro');
215
216     %If no KF used
```

```
217     else
218         X_temp = X;
219         if (meas_occur)
220         X = [Z(1); Z(2); 0.1; 0.1];
221         else
222         X = [Z_prev(1); Z_prev(2); 0.1; 0.1];
223         end
224     end
225     % Determine rotational disturbance angle contribution
226     [disturbance_contribution, beamwidth] = disturbance(X(1), X_true
            (1,k),Z_buff(1,k), blink, adaptcontrol, plotlens, thetadis);
227
228     X(1) = disturbance_contribution;
229     beamwidth_buff(k) = beamwidth;
230
231 %     X(1) = X(1) + disturbance_contribution;
232
233      % True vel
234         Vel = (X_true(:,k)- Xt_prev)/del_t;
235         X_buff(:,k) = X([1 2]);
236      % Updating velocity buff
237         VE_buff(:,k) = X([3 4]);
238      % Error of target to true position, with 1 interval delay to
            mimic
239      % processing delays
240         E_buff(:,k) = abs(X_true(:,k)-X_prev([1 2]));
241         norm_error(k) = norm(E_buff(:,k));
242         K_buff(k) = norm(K);
243         X_prev = X;
244         Xt_prev = [X_true(:,k)];
245         P_buff(k) = norm(P, 'fro');
246
247
248         %% PV cell recieved power
249
250        % Laser image size on implant
251        sigma = beamwidth*precision;
252        % Adding new elements to misalignment arrays
253        misx(k) = (precision*horzeyeradius)*tand(E_buff(1,k));
254        misy(k) = (precision*verteyeradius)*tand(E_buff(2,k));
255        % Finding total power on cell
256          for i=1:1:size  for j=1:1:size
257            beam(i,j)=maxpower*exp(-((i-halfsize-misx(k))^2/(2*sigma
```

```
                ^2))-(j-halfsize-misy(k))^2/(2*sigma^2));
258             %don't count the power that doesn't land on the PV cell
259              if(abs(halfsize-i)<pvcellwidth/2 && abs(halfsize-j)<
                    pvcelllength/2)
260                 cell(i,j)=1;
261              else
262                 cell(i,j)=0;
263              end
264          end
265      end
266      %Add up all the power collected
267      pvcellpower=pvefficiency*cell.*beam;
268      if (any(isnan(misx(k))))
269          totalpower(k) = 0;
270      else
271      totalpower(k)=sum(pvcellpower(:))/(size/domainsize)^2;
272      end
273      % Average power calc over the 'safe' amount of time
274      if ((range+1)>k)
275          avg_power(k) = mean(totalpower(1:k));
276      else
277          avg_power(k) = mean(totalpower((k-range):k));
278      end
279  end
280  %% Store totalpower arrays into buffers for later use
281  if m == 1
282      totalpowerwithout = totalpower;
283  elseif m ==2
284      totalpowerwith = totalpower;
285  end
286
287  end
288
289  % % Animation of generator only
290  % true_motion = animatedline('Color', 'b', 'Marker', 'o');
291  % % Loop to animate
292  % for k = 1:length(X_buff(1,:))
293  % addpoints(true_motion,X_buff(1,k),X_buff(2,k));
294  % drawnow
295  % pause(0.01)
296  % end
297
298  %% Analysis of Position for X coord
```

```
% figure;
% p1 = plot(t,Xt_buff(1,:),'g');
% hold on;
% p2 = plot(t,Z_buff(1,:),'b');
% p3 = plot(t,X_buff(1,:),'r');
% p4 = plot(t,VE_buff(1,:),'o');
% title('X-Position estimation');
% xlabel('Time(s)');
% ylabel('Position(micro-m)');
%
% hold off;
% legend('True position','Measurements','Kalman Displacement estimate
    ','X-Velocity');

%% Plot of X_true and X_buff
% Figure
% p5 = plot(X_true(1,:),X_true(2,:),'b');
% hold on;
% p6 = plot(X_buff(1,:),X_buff(2,:),'-o');
% title('Kalman Filter Pupil Tracking');
% xlabel('X Coordinate (micro-m)');
% ylabel('Y Coordinate (micro-m)');
% hold off;
% legend('True State','Estimated state');

% Animation
% vid debug
% de_frames = 500;
% real_time = de_frames/Hz;

% Video Initiliazation
% v = VideoWriter('pupil_motion.avi');
% v.FrameRate = de_frames/real_time;
% open(v);
% % Animated lines
% true_motion = animatedline('Color', 'b', 'Marker', 'o');
% pred_motion = animatedline('Color', 'g', 'Marker', 'x');
% meas_motion = animatedline('Color', 'r', 'Marker', '.');
%
% % Loop to animate
% for k = 1:length(X_true(1,:))
% addpoints(pred_motion,X_buff(1,k),X_buff(2,k));
% addpoints(true_motion,X_true(1,k),X_true(2,k));
```

```
% addpoints(meas_motion,Z_buff(1,k),Z_buff(2,k));
% title({['Time: ',num2str((k*del_t)),' s']});
% drawnow
% % frame = getframe(gcf);
% % writeVideo(v,frame);
% pause(0.01);
% axis([-15 15 -10 10]);
% end

%% Keep last X frames
% Animated lines
% true_motion = animatedline('Color', 'b', 'Marker', 'o');
% pred_motion = animatedline('Color', 'g', 'Marker', 'x');
% meas_motion = animatedline('Color', 'r', 'Marker', '.');

% figure('units', 'normalized', 'outerposition', [0 0 1 1]);
%length of time
limtime = 10;
a = 36;
b = 12;
[elip_x, elip_y] = drawellipse(a,b);
elip_z = ones(1,length(elip_x));
% Loop to animate

 if (animationmotion)
    th = 0:pi/50:2*pi;

 for k = limtime:(length(X_true(1,:))-limtime)
%
% %
% %
% % plot3(elip_x,elip_y,elip_z)
% % hold on;
% % % True state
% % phi = X_true(1,[k:k+limtime]);
% % theta = X_true(2,[k:k+limtime]);
% % rho = 12;
% % a=rho*sin(phi).*cos(theta);
% % b=rho*sin(phi).*sin(theta);
% % c=rho*cos(phi);
% % plot3(a,b,c,'b-o')
% %
% % % Predicted state
```

```
384 % % phi = X_buff(1,[k:k+limtime]);
385 % % theta = X_buff(2,[k:k+limtime]);
386 % % a=rho*sin(phi).*cos(theta);
387 % % b=rho*sin(phi).*sin(theta);
388 % % c=rho*cos(phi);
389 % % plot3(a,b,c,'r-x')
390 % %
391 % % % Measured state
392 % % phi = Z_buff(1,[k:k+limtime]);
393 % % theta = Z_buff(2,[k:k+limtime]);
394 % % a=rho*sin(phi).*cos(theta);
395 % % b=rho*sin(phi).*sin(theta);
396 % % c=rho*cos(phi);
397 % % plot3(a,b,c,'g-*')
398 %
399 %
400 plot(elip_x, elip_y);
401 hold on;
402 plot(X_true(1,[k:k+limtime]), X_true(2,[k:k+limtime]), 'b', '
       MarkerSize', 7);
403 plot(X_buff(1,[k:k+limtime]), X_buff(2,[k:k+limtime]), 'g', '
       MarkerSize', 7);
404 plot(Z_buff(1,[k:k+limtime]), Z_buff(2,[k:k+limtime]), 'r', '
       MarkerSize', 12);
405
406 xunit = beamwidth_buff(k) * cos(th) +  X_buff(1,[k+limtime]);
407 yunit = beamwidth_buff(k) * sin(th) +  X_buff(2,[k+limtime]);
408 plot(xunit,yunit, 'g');
409
410 xunit = 3 * cos(th) +  X_true(1,[k+limtime]);
411 yunit = 3 * sin(th) +  X_true(2,[k+limtime]);
412 plot(xunit,yunit, 'b');
413
414 xunit = 3 * cos(th) +  Z_buff(1,[k+limtime]);
415 yunit = 3 * sin(th) +  Z_buff(2,[k+limtime]);
416 plot(xunit,yunit, 'r');
417
418
419 hold off;
420 axis([-30 30 -15 15]);
421 daspect([1 1 1])
422 title({['Time: ',num2str((k*del_t)),' s']});
423 pause(0.005)
```

```
424 end
425 %
426 % % frame = getframe(gcf);
427 % % writeVideo(v,frame);
428 %
429 end
430
431 % % % POWER Animation
432 % % vid debug
433 % % de_frames = 500;
434 % % real_time = de_frames/Hz;
435 % %
436 % % Video Initiliazation
437 % % v = VideoWriter('pupil_motion.avi');
438 % % v.FrameRate = de_frames/real_time;
439 % % open(v);
440 % % Animated lines
441 % % power = animatedline('Color', 'b', 'Marker', 'x');
442 % % Loop to animate
443 % % for k = 1:length(X_true(1,:))
444 % %
445 % %     addpoints(power,k,totalpower(k));
446 % % title({['Time: ',num2str((k*del_t)),' s']});
447 % % drawnow
448 % % pause(0.01);
449 % % end
450
451 % P_buff = 100*(P_buff/norm(P_buff));
452 % totalpower = totalpower/norm(totalpower);
453 % avg_power = avg_power/norm(avg_power);
454 totalpowerwith = totalpowerwith*0;
455 if (powerplot)
456     % Analysis of Power over time
457     t = 0:del_t:(n-1)*del_t;
458     figure;
459     p1 = plot(t,totalpowerwithout(1:(n)),'g', 'LineWidth', 1.5);
460     hold on;
461 %     coef = polyfit(t, totalpowerwithout(1:(n)),1);
462 %     fit_without = polyval(coef,t);
463 %     p3 = plot(t,fit_without(1:(n)),'b');
464     p2 = plot(t,totalpowerwith(1:(n)),'k','LineWidth', 1.25);
465 %     coef = polyfit(t, totalpowerwith(1:(n)),1);
466 %     fit_with = polyval(coef,t);
```

```
467 %     p4 = plot(t,fit_with(1:(n)),'b');
468 %     p3 = plot(t,totalpower_no_d(1:(n)),'g', 'LineWidth', 0.25);
469     hold off;
470 %     p2 = plot(t,avg_power(1:(n)),'r');
471     % p3 = plot(t,P_buff,'g');
472 %     hold off;
473
474     title({'Power delivered to retinal implant' ; strcat('Horizontal
            angular disturbance =  ', num2str(thetadis_orig), char(176))})
            ;
475     xlabel('Time (s)');
476     ylabel('Power captured by PV cell (mW)');
477     % Set Tick Marks
478     grid on
479     set(gca,'GridLineStyle','--')
480     set(gca,'XTick',0:t(end));
481     set(gca,'YTick',0:10);
482     axis([0 t(end) 0 inf])
483
484     legend('No Reset','With Reset');
485 end
486 %Compare P_norm to average power
487 if (Pnormplot)
488     % Normalize elements
489     P_buff = (P_buff-min(P_buff))/(max(P_buff)-min(P_buff));
490     avg_power = (avg_power-min(avg_power))/(max(avg_power)-min(
            avg_power));
491     totalpower = (totalpower-min(totalpower))/(max(totalpower)-min(
            totalpower));
492     % Analysis of Power over time
493     t = 0:del_t:(n-1)*del_t;
494     figure;
495     p1 = plot(t,P_buff(1:(n)),'b');
496     hold on;
497     p2 = plot(t,avg_power(1:(n)),'r');
498     p3 = plot(t,totalpower(1:(n)),'g');
499     p4 = plot(t, X_blinks(1:(n)),'k.', 'Linewidth', 2);
500     hold off;
501     title('Matrix Norm vs Avg Power over 440 ms');
502     xlabel('Time(s)');
503     ylabel('Norm Magnitude');
504     legend('P_Norm', '440 ms Power Average', 'Instant Power', 'Blink'
            );
```

```
505
506     %% Automated better figs
507 % Defaults
508 width = 6;      % Width in inches
509 height = 4;     % Height in inches
510 alw = 0.75;     % AxesLineWidth
511 fsz = 14;       % Fontsize
512 lw = 0.8;       % LineWidth
513 msz = 8;        % MarkerSize
514
515 % The properties we've been using in the figures
516 set(0,'defaultLineLineWidth',lw);   % set the default line width to
       lw
517 set(0,'defaultLineMarkerSize',msz); % set the default line marker
       size to msz
518 set(0,'defaultLineLineWidth',lw);   % set the default line width to
       lw
519 set(0,'defaultLineMarkerSize',msz); % set the default line marker
       size to msz
520
521 % Set the default Size for display
522 defpos = get(0,'defaultFigurePosition');
523 set(0,'defaultFigurePosition', [defpos(1) defpos(2) width*100, height
       *100]);
524
525 % Set the defaults for saving/printing to a file
526 set(0,'defaultFigureInvertHardcopy','on'); % This is the default
       anyway
527 set(0,'defaultFigurePaperUnits','inches'); % This is the default
       anyway
528 defsize = get(gcf, 'PaperSize');
529 left = (defsize(1)- width)/2;
530 bottom = (defsize(2)- height)/2;
531 defsize = [left, bottom, width, height];
532 set(0, 'defaultFigurePaperPosition', defsize);
533 end
534 % %
535 % filename = 'Conservative1.5mm24HzSampleRate.xlsx'
536 % xlswrite(filename,totalpower',1)
537 %
538 % % Analysis of Power over time
539 % % t = 0:del_t:(n-1)*del_t;
540 % % figure;
```

```
541 % % p1 = plot(t,P_buff(1:(n)),'b');
542 % % hold on;
543 % % p2 = plot(t,K_buff(1:n),'r');
544 % % title('Error Covariance over time');
545 % % xlabel('Time(s)');
546 % % ylabel('Norm');
547 % % legend('P Norm', 'K Norm');
548
549 % % Plot Minimum avg power as a function of Q
550 % figure;
551 % semilogx(Q_buff(:),AP_buff(:));
552 % title('Minimum Average Power versus Logarithm of Process Noise
       Covariance');
553 % xlabel('Process Covariance (Log(mm))')
554 % ylabel('Minimum Average Power over 300 ms (W)')
555 % grid on;
556 end
```

Appendix C

Tracking Pupil Using Image Processing

C.1 Capturing eye motion data

This method was developed by Ross Cheriton of the University of Ottawa's SUN-LAB. It is described here for the sake of clarity.

For the purpose of simulating the system with realistic data, real eye motion samples were recorded by low cost video cameras found in typical smart phones. The method by which the eye motion samples were captured was purposefully simple and low tech, as the motion samples are not required to be high resolution or with high framerate. With a low image resolution of 240p, and a video framerate of 120 frames per second, the videos were sufficient to capture the motion of the eye as it moves about. The resulting measurements of the 2D angular position $\mathbf{z}_k$ are either used directly for the state vector calculation $\mathbf{x}_k$, or to calculate the Kalman filter state estimate $\hat{\mathbf{x}}_{k|k}$.

To capture the eye motion samples, the recorded volunteers simply rested their chins onto a head level, and watched a video displayed on a monitor. The recording camera was placed in a position that the straight ahead gaze would place the pupil in the center of the image, and the eye globe would take up as much of the image as possible while maintaining focus. The time series of the pupil position on the eye globe was extracted from the video with a pupil edge detection MATLAB program that would determine the center of the pupil within each frame [58]. By observation, the measured pupil center coordinates that were calculated from the eye motion sample were found to have an error of no more than 2° deviation from

the true position of the pupil within the image. The program code can be found in the appendix C. A sample output of the program tracking the pupil center is shown in Figure C.1.

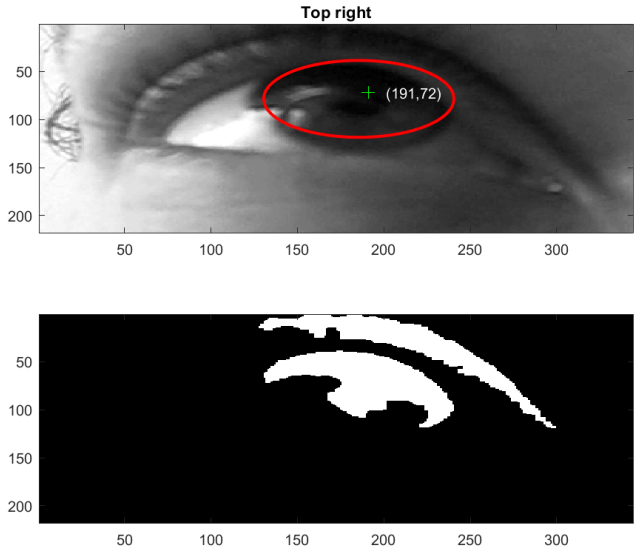

Figure C.1: A sample of the image processing code overlaying an ellipse centered on the pupil. The pixel coordinates of the pupil center are transformed into the corresponding coordinates of the eye gaze.

In well-lit conditions where the recorded volunteer did not move around, the program would never fail to draw an ellipse about the pupil or iris. The program is also capable of skipping video frames where it determines no pupil edge is detectable, which proves useful during eye blink events.

Large errors in the estimate of the pupil center arise during situations where the volunteer would blink, resulting in temporary incorrect circles being drawn about false pupil edges (e.g. the corners of the eye where the tear ducts are located). These errors were never sustained for more than 1 to 2 frames (a time interval no greater than 17 ms). Figure C.2 shows an example of where a large error in measurement occurs while utilizing a standard eye tracking program. By selecting the correct parameters for the Kalman filter described in Section 3.3, the impact of large sporadic errors may be nullified.

A similar camera-based pupil detection camera image processing method is used with the experimental prototype implant tracking system described in Section 3.6. A high speed takes video camera takes images of an imitation eye at a rate of 60 frames per second (fps). The embedded CPU on the camera board ap-

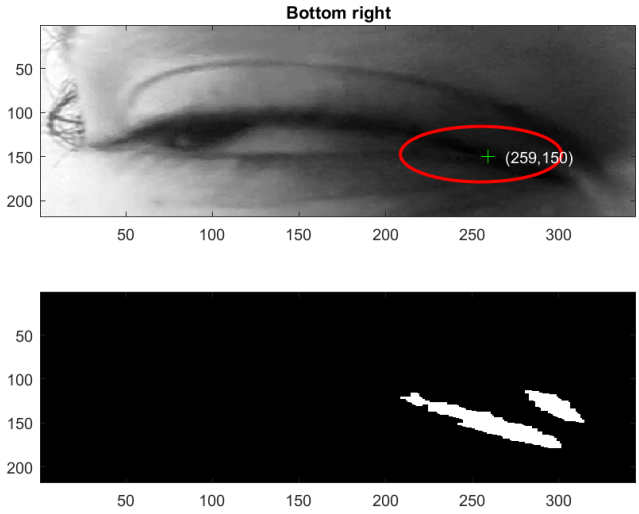

Figure C.2: An example of a blink event resulting in a large measurement error.

plies a pupil edge detection algorithm, which is able to measure coordinates for the center of the pupil in real-time with a delay of less than 20 ms.

C.2 Pupil tracking code with MATLAB

This program was originally published as found in [58], with minor modifications.

Listing C.1: Pupil tracking code with Matlab

```
obj = VideoReader('EditBlinkMove.mov');
NumberOfFrames = obj.NumberOfFrames;
%
la_imagen=read(obj,10);
filas=size(la_imagen,1);
columnas=size(la_imagen,2);
% Center
centro_fila=round(filas/2);
centro_columna=round(columnas/2);
 figure(1);
 XY =[];
 % % Video Initiliazation

v = VideoWriter('EditBlinkMove.avi');
v.FrameRate = 24;
```

```
16 open(v);
17
18 for cnt = 1:NumberOfFrames
19     la_imagen=read(obj,cnt);
20     if size(la_imagen,3)==3
21         la_imagen=rgb2gray(la_imagen);
22     end
23
24     subplot(212)
25     piel=¬im2bw(la_imagen,0.19);
26     %     --
27     piel=bwmorph(piel,'close');
28     piel=bwmorph(piel,'open');
29     piel=bwareaopen(piel,200);
30     piel=imfill(piel,'holes');
31     imagesc(piel);
32     % Tagged objects in BW image
33     L=bwlabel(piel);
34     % Get areas and tracking rectangle
35     out_a=regionprops(L);
36     % Count the number of objects
37     N=size(out_a,1);
38     if N < 1 || isempty(out_a) % Returns if no object in the image
39         % Select larger area
40     areas=[out_a.Area];
41     [area_max pam]=max(areas);
42     subplot(211)
43     imagesc(la_imagen);
44     colormap gray
45     hold on
46     hold off
47     % --
48     drawnow;
49     frame = getframe(gcf);
50     writeVideo(v,frame);
51     XY(cnt,:) = [NaN,NaN];
52
53     else
54         % Select larger area
55     areas=[out_a.Area];
56     [area_max pam]=max(areas);
57     subplot(211)
58     imagesc(la_imagen);
```

```
59      colormap gray
60      hold on
61      rectangle('Position',out_a(pam).BoundingBox,'EdgeColor',[1 0
            0],...
62          'Curvature', [1,1],'LineWidth',2)
63      centro=round(out_a(pam).Centroid);
64      X=centro(1);
65      Y=centro(2);
66      plot(X,Y,'g+')
67      %
68      text(X+10,Y,['(',num2str(X),',',num2str(Y),')'],'Color',[1 1 1])
69      if X<centro_columna && Y<centro_fila
70          title('Top left')
71      elseif X>centro_columna && Y<centro_fila
72          title('Top right')
73      elseif X<centro_columna && Y>centro_fila
74          title('Bottom left')
75      else
76          title('Bottom right')
77      end
78      hold off
79      % --
80      drawnow;
81      frame = getframe(gcf);
82      writeVideo(v,frame);
83      XY(cnt,:) = [X,Y];
84
85      end
86  end
87  close(v);
```

Bibliography

[1] Seth R Flaxman et al. "Global causes of blindness and distance vision impairment 1990-2020: a systematic review and meta-analysis". eng. In: *The Lancet Global Health* 5.12 (Dec. 2017), e1221–e1234. ISSN: 2214-109X.

[2] Karen M. Gehrs et al. "Age related macular degeneration: emerging pathogenetic and therapeutic concepts". eng. In: *Annals of Medicine* 38.7 (Jan. 2006), pp. 450–471. ISSN: 0785-3890.

[3] Dyonne T Hartong, Eliot L Berson, and Thaddeus P Dryja. "Retinitis pigmentosa". eng. In: *The Lancet* 368.9549 (2006), pp. 1795–1809. ISSN: 0140-6736.

[4] Mark S Humayun et al. "Visual Perception Elicited by Electrical Stimulation of Retina in Blind Humans". eng. In: *Archives of Ophthalmology* 114.1 (Jan. 1996), pp. 40–46. ISSN: 0003-9950.

[5] S Sekhar et al. "Tickling the retina: integration of subthreshold electrical pulses can activate retinal neurons". eng. In: *Journal of Neural Engineering* 13.4 (Aug. 2016). ISSN: 1741-2560.

[6] D.L. Cheng, P.B. Greenberg, and D.A. Borton. "Advances in Retinal Prosthetic Research: A Systematic Review of Engineering and Clinical Characteristics of Current Prosthetic Initiatives". In: *Current Eye Research* 42.3 (2017), pp. 334–347. DOI: 10.1080/02713683.2016.1270326.

[7] Yvonne H.-L. Luo and Lyndon da Cruz. "A review and update on the current status of retinal prostheses (bionic eye)". In: *British Medical Bulletin* 109.1 (Mar. 2014), pp. 31–44. ISSN: 0007-1420.

[8] Alice T Chuang, Curtis E Margo, and Paul B Greenberg. "Retinal implants: a systematic review". eng. In: *British Journal of Ophthalmology* 98.7 (July 2014). ISSN: 0007-1161. URL: http://bjo.bmj.com/content/98/7/852.full.pdf.

[9] Philip M. Lewis et al. "Advances in implantable bionic devices for blindness: a review". In: *ANZ Journal of Surgery* 86.9 (Sept. 2016), pp. 654–659. ISSN: 1445-1433.

[10] Susanne Klauke et al. "Stimulation with a wireless intraocular epiretinal implant elicits visual percepts in blind humans". eng. In: *Investigative ophthalmology & visual science* 52.1 (Jan. 2011). ISSN: 1552-5783.

[11] A. Ahnood et al. "Ultrananocrystalline diamond-CMOS device integration route for high acuity retinal prostheses". eng. In: *Biomedical Microdevices* 17.3 (June 2015), pp. 1–11. ISSN: 1387-2176.

[12] Alex E. Hadjinicolaou et al. "Electrical stimulation of retinal ganglion cells with diamond and the development of an all diamond retinal prosthesis". eng. In: *Biomaterials* 33.24 (Aug. 2012), pp. 5812–5820. ISSN: 0142-9612.

[13] J O Mills, A Jalil, and P E Stanga. "Electronic retinal implants and artificial vision: journey and present". In: *Eye* 31.10 (May 2017). ISSN: 0950-222X.

[14] Philip M. Lewis et al. "Restoration of vision in blind individuals using bionic devices: A review with a focus on cortical visual prostheses". eng. In: *Brain Research* 1595 (Jan. 2015), pp. 51–73. ISSN: 0006-8993.

[15] Eberhart Zrenner. "Fighting blindness with microelectronics". eng. In: *Science translational medicine* 5.210 (Nov. 2013). ISSN: 1946-6242.

[16] Howard W. Francis et al. "Impact of Cochlear Implants on the Functional Health Status of Older Adults". eng. In: *Laryngoscope* 112.8 (Aug. 2002), pp. 1482–1488. ISSN: 0023-852X.

[17] Jelmer van Schoonhoven et al. "The effectiveness of bilateral cochlear implants for severe-to-profound deafness in adults: a systematic review". eng. In: *Otology & neurotology : official publication of the American Otological Society, American Neurotology Society [and] European Academy of Otology and Neurotology* 34.2 (Feb. 2013). ISSN: 1537-4505.

[18] S. Khandhadia et al. "Age-related macular degeneration and the complement system". In: *Immunobiology* 217.2 (2012), pp. 127–146. ISSN: 0171-2985. DOI: https://doi.org/10.1016/j.imbio.2011.07.019.

[19] Tracy Hampton. "Gene Therapy for Blindness". eng. In: *JAMA* 303.13 (Apr. 2010), pp. 1245–1245. ISSN: 0098-7484.

[20] G. Dagnelie et al. "Performance of real-world functional vision tasks by blind subjects improves after implantation with the Argus II retinal prosthesis system". In: *Clinical and Experimental Ophthalmology* 45.2 (2017), pp. 152–159. DOI: 10.1111/ceo.12812.

[21] K. Stingl et al. "Artificial vision with wirelessly powered subretinal electronic implant alpha-IMS". In: *Proceedings of the Royal Society B: Biological Sciences* 280.1757 (2013). DOI: 10.1098/rspb.2013.0077.

[22] Alfred L. Yarbus. *Eye Movements and Vision*. Translation to English by Basil Haigh, Lorrin A Riggs (orig. publish date of 1965.) Plenum Press, 1967.

[23] Richard E. Woods Rafael C. Gonzales. *Digital Image Processing*. second. Prentice Hall, 2001.

[24] Veronica Sundstedt. *Gazing at Games: An Introduction to Eye Tracking Control*. Synthesis Lectures on Computer Graphics and Animation. Morgan & Claypool, 2012. DOI: 10.2200/S00395ED1V01Y201111CGR014.

[25] H Davson. *Physiology of the Eye*. fourth. New York: Academic Press, 1980.

[26] Andrew Duchowski. *Eye Tracking Methodology*. second. ISBN 978-1-84628-608-7. Springer, 2007.

[27] David Noton and Lawrence Stark. "Eye Movements and Visual Perception". In: *Scientific American* 224.6 (June 1971). ISSN: 0036-8733.

[28] David Noton and Lawrence Stark. "Scanpaths in saccadic eye movements while viewing and recognizing patterns". eng. In: *Vision Research* 11.9 (1971), 929, IN3–942, IN8. ISSN: 0042-6989.

[29] V Laurutis and Da Robinson. "The vestibulo-ocular reflex during human saccadic eye movements." eng. In: *Journal of Physiology (London)* 373 (Jan. 1986), pp. 209–233. ISSN: 0022-3751. URL: http://search.proquest.com/docview/14786895/.

[30] A F Fuchs, C R Kaneko, and C A Scudder. "Brainstem control of saccadic eye movements". eng. In: *Annual review of neuroscience* 8 (1985). ISSN: 0147-006X.

[31] R W Baloh et al. "Quantitative measurement of saccade amplitude, duration, and velocity". eng. In: *Neurology* 25.11 (Nov. 1975). ISSN: 0028-3878.

[32] D.A. Robinson. "The oculomotor control system: A review". eng. In: *Proceedings of the IEEE* 56.6 (June 1968), pp. 1032–1049. ISSN: 0018-9219.

[33] David E. Irwin. "Visual Memory Within and Across Fixations". In: *Eye Movements and Visual Cognition: Scene Perception and Reading*. Ed. by Keith Rayner. New York, NY: Springer New York, 1992, pp. 146–165. ISBN: 978-1-4612-2852-3. DOI: 10.1007/978-1-4612-2852-3_9.

[34] Serge Meimon et al. "Pupil motion analysis and tracking in ophthalmic systems equipped with wavefront sensing technology". In: *Appl. Opt.* 56.9 (Mar. 2017), pp. D66–D71. DOI: 10.1364/AO.56.000D66.

[35] R M Pritchard. "Stabilized images on the retina". eng. In: *Scientific American* 204 (June 1961). ISSN: 0036-8733.

[36] Jorge Otero Millan et al. "Triggering mechanisms in microsaccade and saccade generation: a novel proposal". In: *Annals of the New York Academy of Sciences* 12331.1 (Sept. 2011), pp. 107–116. ISSN: 0077-8923.

[37] H Collewijn, J van Der Steen, and R M Steinman. "Human eye movements associated with blinks and prolonged eyelid closure". eng. In: *Journal of neurophysiology* 54.1 (July 1985). ISSN: 0022-3077.

[38] Frans Vanderwerf et al. "Eyelid movements: behavioral studies of blinking in humans under different stimulus conditions". eng. In: *Journal of neurophysiology* 89.5 (May 2003). ISSN: 0022-3077.

[39] Andrew T. Duchowski. "Gaze-based interaction: A 30 year retrospective". eng. In: *Computers & Graphics* 73 (June 2018), pp. 59–69. ISSN: 0097-8493.

[40] A. Caspi et al. "Eye movement control in the Argus II retinal-prosthesis enables reduced head movement and better localization precision". In: *Investigative Ophthalmology and Visual Science* 59.2 (2018), pp. 792–802. DOI: 10.1167/iovs.17-22377.

[41] Arman Ahnood et al. "Retinal Implants: Diamond Devices for High Acuity Prosthetic Vision (Adv. Biosys. 1-2/2017)". In: *Advanced Biosystems* 1.1-2 (). DOI: 10.1002/adbi.201770001.

[42] N. L. Opie et al. "Heating of the Eye by a Retinal Prosthesis: Modeling, Cadaver and In Vivo Study". eng. In: 59.2 (2012), pp. 339–345. ISSN: 0018-9294.

[43] Veljko Milanović. "Device for optical imaging, tracking, and position measurement with a scanning MEMS mirror". US8427657B2. 2013.

[44] *Mirrorcle Technologies, Inc. - Photo Gallery*. https://www.mirrorcletech.com/photo.html. Accessed on September 27, 2018.

[45] PR Patterson et al. "Scanning micromirrors: An overview". In: *Optomechatronic Micro/Nano Components, Devices, and Systems*. Ed. by Katagiri, Y. Vol. 5604. Proceedings of SPIE. Conference on Optomechatronic Micro/Nano Components, Devices and Systems, Philadelphia, PA, OCT 27-28, 2004. SPIE; IEICE Commun Soc; IEICE Elect Soc. 2004, 195–207. ISBN: 0-8194-5557-1. DOI: 10.1117/12.582849.

[46] Robert Moss et al. "Low-cost compact MEMS scanning LADAR system for robotic applications". In: *Laser Radar Technology and Applications XVII*. Ed. by Turner, MD and Kamerman, GW. Vol. 8379. Proceedings of SPIE. Conference on Laser Radar Technology and Applications XVII, Baltimore, MD, APR 24-26, 2012. SPIE. 2012. ISBN: 978-0-8194-9057-5. DOI: 10.1117/12.919804.

[47] V. Milanović et al. "A fast single-pixel laser imager for VR/AR headset tracking". In: *Society of Photo-Optical Instrumentation Engineers (SPIE) Conference Series*. Vol. 10116. Society of Photo-Optical Instrumentation Engineers (SPIE) Conference Series. Feb. 2017, 101160E. DOI: 10.1117/12.2253425.

[48] Veljko Milanovic et al. "Closed-Loop Control of Gimbal-less MEMS Mirrors for Increased Bandwidth in LiDAR Applications". In: *Laser Radar Technology and Applications XXII*. Ed. by Turner, MD and Kamerman, GW. Vol. 10191. Proceedings of SPIE. Conference on Laser Radar Technology and Applications XXI, Anaheim, CA, APR 11-12, 2017. SPIE. 2017. ISBN: 978-1-5106-0883-2; 978-1-5106-0884-9. DOI: 10.1117/12.2264069.

[49] Veljko Milanovic, Abhishek Kasturi, and James Yang. "Novel Fluidic Packaging of Gimbal-less MEMS Mirrors for Increased Optical Resolution and Overall Performance". In: *Micro- and Nanotechnology Sensors, Systems, and Applications VIII*. Ed. by George, T and Dutta, AK and Islam, MS. Vol. 9836. Proceedings of SPIE. Conference on Micro- and Nanotechnology Sensors, Systems, and Applications VIII, Baltimore, MD, APR 17-21, 2016. SPIE. 2016. ISBN: 978-1-5106-0077-5. DOI: 10.1117/12.2224377.

[50] Rudolf Kalman. "A New Approach To Linear Filtering and Prediction Problems". In: *Journal of Basic Engineering (ASME)* 82D (Jan. 1960), pp. 35–45.

[51] V Varsha, Radhakant Padhi, and Aditya Murthy. "A Stochastic Feedback Model to Simulate Saccadic Eye Movement Variability." In: *IFAC-PapersOnLine* 50.1 (2017). 20th IFAC World Congress, pp. 13521–13525. ISSN: 2405-8963. DOI: https://doi.org/10.1016/j.ifacol.2017.08.2344.

[52] Adam Charles. *Kalman Filtering: A Bayesian Approach*. https://adamsc.mycpanel.princeton.edu/documents/KalmanFilterBayesDerivation.pdf. Accessed on September 27, 2018.

[53] Aurélien Valade et al. "A Study about Kalman Filters Applied to Embedded Sensors". In: *Sensors* 17.12 (2017). ISSN: 1424-8220. DOI: 10.3390/s17122810. URL: http://www.mdpi.com/1424-8220/17/12/2810.

[54] Inessa Bekerman, Paul Gottlieb, and Michael Vaiman. "Variations in Eyeball Diameters of the Healthy Adults". eng. In: *Journal of Ophthalmology* 2014.2 (2014). ISSN: 2090-004X.

[55] Ioannis Rigas, Oleg Komogortsev, and Reza Shadmehr. "Biometric Recognition via Eye Movements: Saccadic Vigor and Acceleration Cues". eng. In: *ACM Transactions on Applied Perception (TAP)* 13.2 (2016), pp. 1–21. ISSN: 1544-3558.

[56] Violet Mwaffo et al. "A jump persistent turning walker to model zebrafish locomotion". eng. In: *Journal of the Royal Society of London Interface* 12.102 (2015), pp. 20140884–20140884. ISSN: 1742-5689.

[57] Erik D. Reichle and Patryk A. Laurent. "Using Reinforcement Learning to Understand the Emergence of "Intelligent" Eye-Movement Behavior during Reading". eng. In: *Psychological Review* 113.2 (2006), pp. 390–408. ISSN: 0033-295X.

[58] Diego Barragán. *Tracking pupil using image processing. - File Exchange - MATLAB Central*. https://www.mathworks.com/matlabcentral/fileexchange/49599-tracking-pupil-using-image-processing. Accessed on September 27, 2018. Feb. 2015.